Technical University of Denmark

DTU

Dynamic Modeling of Wind Turbine Gearboxes and Experimental Validation

Pedersen, Rune; Santos, Ilmar

Publication date:
2010

Document Version
Publisher's PDF, also known as Version of record

[Link back to DTU Orbit](#)

Citation (APA):
Pedersen, R., & Santos, I. (2010). Dynamic Modeling of Wind Turbine Gearboxes and Experimental Validation. Kgs. Lyngby, Denmark: Technical University of Denmark (DTU). (DCAMM Special Repport; No. S113).

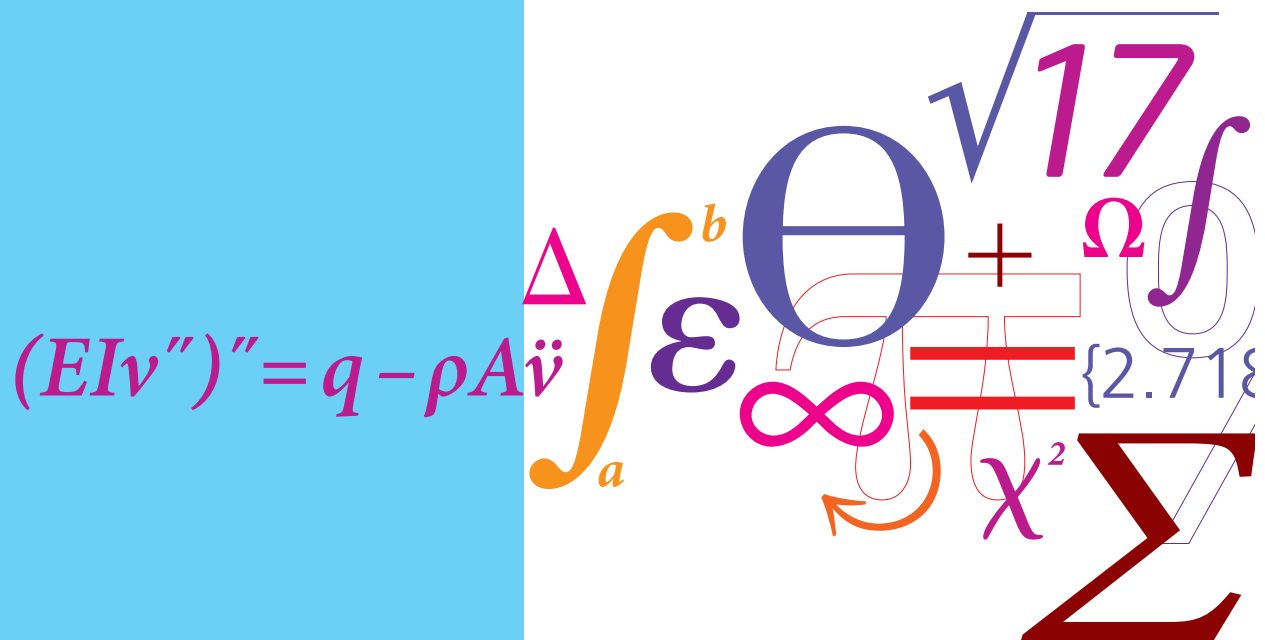**DTU Library**
Technical Information Center of Denmark

Dynamic Modeling of Wind Turbine Gearboxes and Experimental Validation

PhD Thesis

$$(EIv'')'' = q - \rho A\ddot{v}$$

DTU Mechanical Engineering
Department of Mechanical Engineering

Dynamic Modeling of Wind Turbine Gearboxes and Experimental Validation

Rune Pedersen

Monday 26th April, 2010

Contents

Abstract

Grinding corrections are often applied to gear teeth, which will alter the load distribution across the tooth. Grinding corrections will also change the load sharing between neighboring tooth pairs, and in turn the gear mesh stiffness. In this thesis, a model for calculating the gear mesh stiffness is presented. The model takes into account the effects of load and applied grinding corrections. The results are verified by comparing to simulated and experimental results reported in the existing literature. Using gear data loosely based on a 1 MW wind turbine gearbox, the gear mesh stiffness is expanded in a Fourier series and combined with a simple, torsional multibody model. Under the assumption of constant angular velocity of the gears, the methods of time-varying modal analysis are applied to this system. This investigation is carried out in order to evaluate the potential of the time-varying modal analysis in relation to gear dynamics.

A multibody model of two complete 2.3 MW wind turbine gearboxes mounted back-to-back in a test rig is built. The mean values of the proposed gear mesh stiffnesses are included. The model is validated by comparing with calculated and measured eigenfrequencies and mode shapes. The measured eigenfrequencies have been identified in accelerometer signals obtained during run-up tests. Since the calculated eigenfrequencies do not match the measured eigenfrequencies with sufficient accuracy, a model updating technique is applied to ensure a better match by adjusting the model parameters.

Resumé (in Danish)

Slibekorrekturer på tandhjul vil ændre lastfordelingen henover tænderne. Korrekturerne vil også påvirke den måde, hvorpå de enkelte tandpar i indgreb deler den samlede belastning, og derigennem påvirkes indgrebsstivheden. I denne afhandling præsenteres en model for indgrebsstivheden, som medtager afhængigheden af belastning og slibekorrekturer. Resultaterne er verificeret ved sammenligning med beregnede og eksperimentelle data fra den eksisterende litteratur. Under brug af data, der er løst baseret på et 1 MW vindmøllegear, udvikles indgrebsstivheden i en Fourierrække og sættes sammen med en multibody-model, der simulerer systemets torsionssvingninger. Tandhjulene antages at rotere med konstant hastighed, hvilket gør det muligt at anvende teorierne om modalanalyse af periodisk tidsvarierende systemer. Målet er at undersøge den tidsvarierende modalanalyses potentiale i relation til gear-dynamik.

Der er udviklet en multibody-model af to 2.3 MW vindmøllegear sat op mod hinanden på en testbænk. Middelværdierne af de beregnede indgrebsstivheder er inkluderet. Modellen valideres ved sammenligning med beregnede egenfrekvenser og egensvingningsformer, og med målte egenfrekvenser. De målte egenfrekvenser er identificeret fra accelerometermålinger foretaget under run-up tests. Idet de beregnede egenfrekvenser ikke stemmer overens med de målte med tilstrækkelig præcision, er der benyttet en opdateringsteknik til at forbedre de simulerede resultater ved at justere på modelparametrene.

List of symbols

Symbol	Description	Unit
$\mathbf{A}$	State matrix	
$\mathbf{a_0}$	Transverse acceleration of gear	$[\text{m/s}^2]$
a	Measured acceleration	$[\text{m/s}^2]$
a	Centre distance	$[\text{m}]$
B	Normal plane tooth width	$[\text{m}]$
b	Face width	$[\text{m}]$
b	Half width of zone of influence	$[\text{m}]$
b_e	Length of end relief	$[\text{m}]$
$\mathbf{C}$	Damping matrix	
C_1, C_2, C_3	Integration constants	
C_{11}, C_{12}, C_{22}	Gear body deflection constants	
C_a, C_e, C_f	Tip, end, root relief	$[\text{m}]$
C_b, C_h	Lead crowning, profile crowning	$[\text{m}]$
c	Stiffness	$[\text{N/m, Nm/rad}]$
c	Tip clearance	$[\text{m}]$
c_1, c_2	Beam support stiffness	$[\text{N/m, Nm/rad}]$
c_γ	Mean gear mesh stiffness	$[\text{N/(mm·}\mu\text{m)}]$
$\mathbf{d}$	Effective modification vector	$[\text{m}]$
d_a	Tip diameter	$[\text{m}]$
d_f	Root diameter	$[\text{m}]$
E	Young's modulus	$[\text{N/m}^2]$
E_{eff}	Effective Young's modulus	$[\text{N/m}^2]$
$\mathbf{F}$	Vector of generalized forces	$[\text{N,Nm}]$
F	Scalar force	$[\text{N}]$
F	Beam bending stiffness	$[\text{N/m}^2]$
F	Scalar error measure	
$\mathbf{f}$	Vector of generalized forces	$[\text{N,Nm}]$
$\mathbf{f}_A$	Vector of calculated eigenfrequencies	$[\text{Hz}]$
$\mathbf{f}_X$	Vector of measured eigenfrequencies	$[\text{Hz}]$
f	Beam bending deflection	$[\text{m}]$
f	Eigenfrequency	$[\text{Hz}]$
G	Shear modulus	$[\text{N/m}^2]$
H	Tooth thickness	$[\text{m}]$
H_{root}	Normal plane tooth root thickness	$[\text{m}]$

Symbol	Description	Unit
h	Depth of zone of influence	[m]
h_{aP}	Addendum coefficient of basic rack	
h_{aP0}	Addendum coefficient of tool	
$\mathbf{I}$	Identity matrix	
I, I_{MAX}	Tooth grid coordinate, number of grid lines	
I_A	Tooth bending moment of inertia	[m^4
i	Gear ratio	
i	Imaginary unit, $\sqrt{-1}$	
J	Mass moment of inertia	[kgm^2]
J,J_{MAX}	Gear relative position, number of positions	
$\mathbf{K}$	Stiffness matrix	
$\mathbf{K}_J$	Index vector for contacting sections, step J	
K,K_{MAX}	Tooth grid coordinate, number of grid lines	
K_P	Loaded slice	
k	Stiffness	[N/m, Nm/rad]
k_m	Mean gear mesh stiffness	[N/m]
$\mathbf{L}$	Matrix of left eigenvectors	
L	Tooth height	[m]
L	Lagrange function	[J]
L_a, L_f	Length of tip relief, root relief	[m]
$\mathbf{M}$	Mass matrix	
M, M_t	Bending moment, torque	[Nm]
m_n	Normal module	[m]
N_{max}	Max. number of tooth pairs in contact	
P	Force normal to tooth surface, normal plane	[N]
P_R	Radial force, normal plane	[N]
P_S	Shear force, normal plane	[N]
p_{max}	Maximum Hertzian pressure	[N/m^2]
pr_0	Amount of protuberance in tool	[m]
$\mathbf{q}$	Vector of generalized displacements	[m,rad]

Symbol	Description	Unit
q_1, q_2	Normalized single tooth deflections	
q_H	Normalized Hertzian deflection	
$\mathbf{R}$	Matrix of right eigenvectors	
R	Radius for mounting of accelerometers	[m]
$\mathbf{r}$	Right eigenvector	
r	Radius	[m]
r_a	Tip radius	[m]
r_b	Base radius	[m]
r_p	Distance to center of gear	[m]
r_R	Distance to center of gear	[m]
$\mathbf{S}_M$, $\mathbf{S}_K$	Mass, stiffness eigensensitivity matrix	[Hz]
t	Time	[s]
T	Period of oscillation, measurement time	[s]
T	Kinetic energy	[J]
T	Torque	[Nm]
U	Potential energy	[J]
u_K, u_M	Stiffness, mass updating factors	
$\mathbf{v}$	Eigenvector	
$\mathbf{W}$	Model updating weighting functions	
W_0	Line load	[N/m]
$\mathbf{X}$	Generalized deflection vector	[m, rad]
$\mathbf{X}_H$	Hertzian deflection vector	[m]
$\mathbf{X}_T$	Tooth pair bulk deflection vector	[m]
X	Elastic tooth pair deflection	[m]
X	Overlap	per cent
X_n	Effective modifications of tooth pair n	[m]
x	Addendum modification coefficient	
x_E	Generating addendum modification coefficient	
$\mathbf{Y}$	Tooth pair displacement vector	[m]
Y_A	Normal plane Hertzian deflection	[m]

Symbol	Description	Unit
Y_{AE}	Transverse plane Hertzian deflection	[m]
Y_{BE}	Transverse plane tooth bending	[m]
Y_{KE}	Transverse plane gear body deflection	[m]
Y_{KM}	Tooth base rotation	[m]
Y_{KP}	Tooth base translation	[m]
Y_n	Deflection of tooth pair n	[m]
Y_{RE}	Transverse plane tooth compression	[m]
Y_{SchE}	Transverse plane tooth shear	[m]
y_P	Distance from force attack to tooth base	[m]
$\mathbf{Z}$	Tooth compliance matrix	
$\mathbf{Z}_I$	Tooth compliance matrix, I-direction	
$\mathbf{Z}_K$	Tooth compliance matrix, K-direction	
Z	Number of spectral averages	
$\mathbf{z}$	State space coordinates	[rad,rad/s]
z	Number of teeth	

Symbol	Description	Unit
α_{at}	Angle of attack	[rad]
α_n	Normal pressure angle	[rad]
$\alpha_{n,at}$	Normal plane angle of attack	[rad]
α_{pr0}	Protuberance angle	[rad]
α_{wt}	Working transverse pressure angle	[rad]
β, β_b	Helix angle, base helix angle	[rad]
$\Delta\mathbf{f}$	Error in calculated eigenfrequencies	[Hz]
Δf	Frequency resolution	[Hz]
$\epsilon_\alpha, \epsilon_\gamma$	Transverse, total contact ratio	
ζ	Tooth width coordinate	[m]
ζ_P	Force attack coordinate	[m]
η	Normal plane involute profile	[m]
η_B	Normal plane tooth bending	[m]
η_R	Deflection due to compression	[m]
η_S	Transverse plane involute profile	[m]
η_{Sch}	Normal plane tooth shear	[m]
θ	Rotation	[rad]
κ	Timoshenko shear coefficient	
λ	Eigenvalue	
ν	Poisson's ratio	
ξ	Distance from tooth tip	[m]
ξ_P	Force attack coordinate	[m]
ξ_R	Radial tooth deflection	[m]
ρ	Radius of curvature	[m]
ρ_{aP0}	Tip rounding radius of tool	[m]
ρ_f	Root fillet radius	[m]
τ	Relative gear position	
τ	Shear stress	[N/m^2]
ψ	Angle of acceleration vector $\mathbf{a_0}$	[rad]
Ω	Gear mesh frequency, angular velocity	[rad/s]

Abbreviations

DOF   Degree of Freedom
FE   Finite Element
FFT   Fast Fourier Transformation
HSS   High Speed Stage
IMS   Intermediate Speed Stage
LOA   Line of Action
MAC Modal Assurance Criterion
NC   Normalized Compliance
NF   Normalization Factor for mode shapes
RMS   Root-Mean-Square
SAP   Start of Active Profile

Chapter 1

Introduction and Literature Review

Many areas of dynamics and statics are needed when creating a mathematical model of a complete, geared wind turbine drive train. As the main source of excitation is the meshing of the gear teeth, special attention is paid to this subject. As it will later be shown, it makes sense to divide the question of how to model the meshing gears into several subjects: First it will be examined how to calculate the stiffness of the teeth using theory of elasticity. Secondly, the incorporation of the found stiffnesses in the dynamic gear model will be investigated. Since planetary stages, which shows special dynamic behavior, are important parts of a modern wind turbine gear box, existing literature on this subject will also be reviewed. Finally the literature related to model validation will be examined.

1.1 Static Gear Mesh Modeling

The history of explaining gear tooth deflection dates back to 1938, where Walker [1] uses experimental results to predict tooth deformation under load, and uses his results to make recommendations for profile modifications. In 1955, Weber and Banaschek [2] uses the theory of elasticity to explain the gear deformation under load as a function of gear geometry. The total deformation is split up into several contributing effects, such as deformation of the tooth, the deformation of the gear body, and the deformation coming from the Hertzian pressure between mating teeth. Ziegler [3] defines a grid, which

is laid out over the tooth surface, and evaluates the tooth stiffness in the points lying on the line of action. Also, he proposes two ways of combining the stiffnesses of several pairs of teeth in mesh simultaneously: A parallel and a serial connection. Niemann and Winter [4] sum up the research on tooth stiffness conducted until the 1980's. They present an overview of the calculations needed for a stiffness evaluation. They pay some attention to the question of load sharing between the teeth, and also show how to determine the stress distribution along one tooth. The decomposition of the deformation introduced in [2] is also used by Vijayakar [5], who solves the Hertzian pressure part of the contact problem using surface integrals, while the other parts are solved using a finite element(FE) model. Arafa and Megahed [6] use finite elements for the whole of the gear including the contact area, and find that the tooth stiffness is strongly dependent on the number of teeth on the gear.

Some of the results from the articles mentioned have been standardized in ISO-6336 [7]. This ISO standard is partly based on the German standard DIN-3990 [8], and partly on the work of Winter and Podlesnik [9, 10, 11], who explain the simplifications used in ISO-6336. A large part of [9, 10, 11] concerns the tooth load distribution as a function of the gear body geometry. The American AGMA-2001 [12] also covers the area of gear mesh stiffness.

1.2   Dynamic Gear Mesh Modeling

The traditional classification of dynamic gear mesh models is based on the basic dynamic behavior of the model:

- LTI (linear time invariant), used for determination of natural frequencies and mode shapes

- LTV (linear time varying), where the mesh stiffness is usually the time-varying component. Typical results are frequency response functions (FRF) and quasi-static forced responses

- NTV (nonlinear time varying) models can include effects as tooth separation and displacement-dependent mesh stiffness functions

Another possible classification follows from Gregory et al. [13], who show that the excitation from the meshing teeth can be separated into two parts:

The first part concerns the angular displacement, which is always present as a result of the necessary clearance between gear teeth, and imperfections on the gears. This is called "transmission error" (TE). The other part is the change in tooth stiffness, as the gears rotate and the point of attack on the tooth profile changes. In [13], ideas are presented on how to calculate both the TE and the stiffness. In most of the articles mentioned below, the end result of the calculations is the dynamic load on the gear teeth.

As shown by Blankenship and Singh [14], the TE and the mesh stiffness depend on each other, making the dynamic gear mesh modeling very complicated. To simplify the calculations, it is common to use the TE as the only external excitation source, and then use the varying stiffness as a parametric excitation. The validity of this procedure is examined by Velex and Ajmi [15], who mentions the problem of defining TE for helical gears as a limitation. Also the assumption of quasi-stationarity often used in TE-excited models has a disadvantage, as it excludes the possibility of using the model to correctly predict dynamic behaviour in a resonant region. This problem is then partly solved by Kahraman and Singh in [16, 17, 18, 19], who use the methods of nonlinear dynamics for solving the equations of motion in a resonant region of a gear pair with a clearance-type nonlinearity. They use TE as an external excitation, and show both periodic, quasi-periodic and chaotic motion. The effect of the nonlinearity is amplified by introducing the varying mesh stiffness.

The non-TE-excited models are another group of gear mesh models, mainly described by a research group in Aachen, Germany [20, 21, 22, 23] , and another group at INSA de Lyon in France, [24, 25, 26]. In this type of model, no knowledge about the TE is needed before the calculation is performed. Peeken et al. [20, 21, 22, 23] present both purely torsional, torsional-axial, torsional-lateral, and torsional-axial-lateral gear mesh models, which are parametrically excited. It is shown, that the equation of motion for the torsional 1-DOF (degree-of-freedom) system reduces to the Mathieu equation, when the gear mesh stiffness is replaced by a cosine function. The regions of instability for this equation are found analytically. Then, more complicated mesh stiffness functions are introduced via the lowest terms of their Fourier series. A large number of numerical simulations are performed, which clarify the role of many model parameters, i.e. mesh stiffness function, damping, tooth clearance and the introduction of the additional DOFs. The

results from the simulations are given as time series of the dynamic tooth forces, which are examined for resonances.

In [24], Velex and Berthe assume continuous contact between the gear teeth, and solve the equations of motion after splitting these in a stationary part (results from the mean external load) and a dynamic part (from the varying part of the external load). The mesh stiffness is described by a Fourier series in the time domain. They also introduce a way of determining which modes are important for the loading used, based on the spatial distribution of deformation energy. Velex and Maatar [25] extend the model by further investigations concerning the mesh stiffness. They divide the tooth surface into grid points similar to [3], each of which has a constant and predefined stiffness value. In each time step they compute the total mesh stiffness as the sum of those individual grid point stiffnesses that are in contact with the mating tooth. This way of defining the stiffness allows the inclusion of tooth errors in a simple way. The model is validated by comparing the calculated side bands in the response spectrum as a result of the errors with vibration measurements of gears with the same errors. The equations of motion are set up using Lagrange's equations. The following article, [26] by Ajmi and Velex, takes into account the elastic deformation of the gear body, as well as an elastic coupling between the predefined spring coefficients. However, they conclude, that such a complex model is rarely needed in pure dynamic modelling, and that it may be more useful if the results of the dynamic simulation is to be followed by a static analysis, i.e. to determine local stresses.

Küçükay's book from 1987 [27] gives a systematic introduction to the dynamic modeling of geared systems. Küçükay emphasizes the importance of clearly defining the purpose of the model, the frequency range of interest, and especially the sources of excitation. In his modeling, he uses several nodes to model a gear wheel to calculate the load distribution across the teeth. To obtain the equations of motion in a very general way, he proposes an extensive use of structure vectors, which contain information about the geometric couplings between the nodes. Küçükay also gives a brief, qualitative introduction to interpreting the response of a nonlinear system, to stability analysis, and to combination frequencies.

Niemann and Winter [4] also give a fine qualitative description of many influence factors regarding gear box vibration and noise radiation. They show

some typical results, and define levels of vibration, that should be expected under normal operating conditions.

1.3 Planetary Gear Modeling

The modeling of planetary gear trains for dynamic simulations started in the 1970's. Cunliffe et al. [28] set up a torsional-transversal model with different kinds of "mesh elements": A linear (constant stiffness) element used to determine natural frequencies and mode shapes, and a nonlinear element allowing tooth separation is used for time integration of the response. The nonlinear element also includes time-varying stiffness. An important contribution in this work is the classification of the found modes into overall, sun, basic, radial, tangential and torsional modes, depending on the form of the mode shape vector. Seager [29] uses the phase differences between the different meshes to determine conditions for the neutralization of certain modes. The goal is to find a suitable number of teeth on the different gears to prevent mesh-induced vibrations. Botman [30] uses a linear torsional-transversal model with the carrier rotating at constant speed to predict natural frequencies and the corresponding mode shapes. His conclusion is that the non-axisymmetric modes will be suppressed by the carrier rotation.

In 1994, a series of articles is presented by Kahraman, [31, 32, 33, 34]. In [31], the development from single-mesh model to multi-mesh model (i.e., a planetary stage) is described. With the proposed formulation, the different gears can be placed at different angles relative to each other, which influences the phase between the meshes. With [32], Kahraman starts with a simple lumped-parameter torsional-transversal model of a planetary gear stage, which allows for analytical expressions for the lowest natural frequencies. The model from [32] is compared with a more complicated model from [33] to determine those parameters, which allows the use of the simpler model. In [33], time-varying mesh stiffness and the possibility of tooth separation is included, and the load sharing between the planets as a function of several errors are calculated. The model is TE-excited, and the TE is expressed in a Fourier series. The model is extended to six DOFs per node in [34], which allows translation and rotation about all three axes. This model is used to study the effects of planet mesh phasing. The model makes use of a fixed coordinate system, which does not rotate with the planet carrier. This means

that many of the equations controlling the planet gear meshes must be updated in every time step, as the carrier rotates. Because of the computation time needed for this operation, this possibly makes the model less suited for numerical integration in the time domain, although it is possible.

As with the single-mesh models described earlier, also the planetary gears can be modeled without knowledge about the TE. This has been done by Saada and Velex, [35], who propose a torsional-transversal model written in a coordinate system fixed to the planet carrier. The contact between the teeth is modeled as a simplified version of the method used in [25], but with an infinite number of grid points along the tooth, and the summation to find the total mesh stiffness is substituted by an integration. The simplification is that no tooth separation and no partial contact is allowed. In 1996, Velex and Flamand [36] produce a three-dimensional model. As this model possesses a large number of DOFs, a Ritz-type reduction algorithm is proposed. A time-dependent mesh stiffness is used to produce parametric excitation. In [37], Abousleiman and Velex extend the model, which now includes ring gear flexibility. This is done using FE beam and solid elements to model the ring gear. Later, Abousleiman et al. [38] consider planet carrier flexibility, although the conclusion to this work is that carrier flexibility is of secondary importance, compared to ring gear flexibility. The planet bearing stiffness is shown to have a great influence on the load distribution across the gear teeth. A number of relevant parametrical studies are presented to give an overview of planetary gear dynamic behavior as a function of the main model parameters, such as ring gear rim thickness and planet position errors. Also, the ring gear modeling technique is examined to find differences between the solid and the beam elements.

A dynamic, planetary gear version of the static gear mesh modeled in [5] is presented by Parker et al. [39]. Here, a FE grid is laid out over the gear set, while the contact zones are modeled using surface integrals. This combined formulation allows the FE method to be used, as it eliminates the need of en extremely fine mesh in the contact zones. In this way, dynamic simulations become possible. The CPU time needed for the calculations is not reported. The model is a two-dimensional model, and an extension to three dimensions will probably make the calculation time unreasonably long.

In 1999, Lin and Parker [40] propose a planar model of a planetary stage to

examine the mode shape properties. The mode shapes are categorized into rotational, translational and planet modes. For each group, the number of distinct and degenerate natural frequencies are calculated, and the dynamic properties are described. Using these results, Lin and Parker [41] compute the derivatives of the natural frequencies with respect to model parameters such as stiffnesses, masses, and moments of inertia. These derivatives are shown to depend on the potential and kinetic energy distributions in a very simple way. In [42], Lin and Parker find instability regions for the parametric gear mesh excitation, for systems with in-phase or sequentially phased planets, and for systems with symmetrically as well as unsymmetrically spaced planets. Again, using the dynamic mode shape properties, the equations turn out very simple. The influence of possible nonlinearities, such as tooth separation, is briefly mentioned. The work of Lin and Parker is summed up in [43].

Peeters [44] models a full wind turbine drive train consisting of two planetary stages and one parallel stage. He includes flexibility of all the parts of the drive train using the component mode synthesis (CMS) technique described by Craig and Bampton [45]. This allows the internal dynamics of the individual drive train components to enter the overall equations of motion, using an acceptable number of DOFs. However, Peeters does not develop his theory to include an advanced gear mesh model. For this reason, he mainly uses the linear properties of his model to calculate the natural frequencies, and to produce frequency responses. A very interesting part of the article is the discussion of how to integrate the drive train model in a full wind turbine model.

1.4 Validation of Models

A validation of the model is necessary to produce useful simulation results. Typically, accelerometer and/or strain gauge signals are used. When comparing the simulation results to experimentally obtained data, different methods can be used:

1) Direct time series or Fast Fourier Transform (FFT) comparison [25, 27, 28]

2) Frequency response comparison [16, 17, 18, 25]. If the simulation model

is linear, or is easily linearized, the frequency response function (FRF) can be calculated directly. Otherwise, a numerical integration of the equations of motion is performed, the results are transformed into the frequency domain, and an envelope curve is plotted and compared to the corresponding curve for the experiment [46]. Also extraction of modal parameters from experiments belongs to this category ([47], chapter 21, [48])

For the relatively small models (low number of DOFs) used in dynamic modeling, one more possibility for validation is present:

3) Comparison of dynamic behavior (normally natural frequencies and mode shapes) to FE models with a large number of DOFs. Also comparison with other mathematical models from the literature fits into this category [43, 44]

In compact gear boxes, as used in wind turbines, it can be difficult to place measurement devices inside the gear box. Therefore, it will be a great advantage if measurements obtained on the outside of the gear housing can be used for the model validation. In this case, a mathematical model of the housing becomes necessary. As described by Ognjanović and Ćirić-Kostić [49, 50], the modal properties of this housing model has a great influence on the simulation results. Another approach is proposed by Aoyama et al. [51], who use torsional vibration measurements obtained on the output shaft of the gear box to estimate the gear vibrations. In this way, the need for a housing model is eliminated, and the gear vibrations can be related to the measured output shaft vibrations via an experimentally obtained or numerically computed transfer function.

Another problem is described by Chen [52], who shows, that only the lowest torsional modes could be excited in his large-scale torsional test rig. He proposes to solve this problem by changing the position of the exciter to a place, where the expected amplitude of vibration is large, based on a previous modal analysis. This solution works fine in his study of a steam turbine drive train, but may be less suited for the excitation of modes associated with a closed gear box. Chen also produces numerically obtained plots of ODS (Operating Deflection Shape), by running his simulation near a critical speed.

On the other hand, if it is possible to place measurement devices on the rotating parts inside the gear box, the model validation can be done in a more

direct way. One possibility is to place accelerometers on the gear wheels [51]. Another way is to glue strain gauges to the gear body between the teeth, as done by Rebbechi et al. [53] and Oswald et al. [54]. The strain gauge signals can be related to dynamic tooth forces, both in the normal and in the tangential direction (friction forces are tangential to the tooth surface). In [53], it is described how to calculate the "tooth force influence coefficient matrix", which is necessary in the signal processing to obtain the tooth forces. Oswald et al. [54] then use this matrix to validate a 4-DOF torsional model of a spur gear.

1.5   Objectives and Original Contributions

From the literature reviewed, it can be concluded that the stiffness of gear teeth can be found at an almost arbitrary precision, due primarily to the use of FE models. However, the FE models do not necessarily provide the best means for understanding the underlying physics of the problem, which is needed when the results from a static analysis are to be used in a dynamic model. Furthermore, to keep the calculation time to a reasonable level, the data from the static analysis must be condensed, i.e. converted to a lower number of DOFs. When doing this, care must be taken to ensure that no vital information is lost. Clearly, the analytical results from the older references are a great help.

When modeling dynamic systems, the understanding of the basic physical principles becomes even more important than in statics, as it is vital for the interpretation of the mode shapes. This means that the best modeling results do not necessarily come from the model with the highest number of DOFs - the selection of the DOFs and the mathematical formulation of the equations relating the DOFs are equally important.

The validation of models seems to be less developed than the other phases in the modeling process. No single method has been recognized as being the best for all purposes. The selection of validation method for a specific project thus depends on the goal of the project.

Following the literature review above, the main contributions of this research work are:

- The application of time-varying modal analysis to the field of gear dynamics. The advantages and drawbacks of the procedure are evaluated.

- The experimental validation of a theoretical model using measurements performed on a fully instrumented and calibrated multi-megawatt gearbox test rig.

1.6   Structure of this Thesis

The outline of the report is:

Chapter 2: A method of calculating the stiffness of a gear mesh is presented. The results are validated by comparison with theoretical and experimental results form the literature.

Chapter 3: Presentation of the theory of modal analysis of periodically time-varying systems. The theory is applied to a single spur gear pair in order to evaluate the potential of the method within gear dynamics.

Chapter 4: A torsional multibody model of two multi-megawatt gearboxes mounted back-to-back in a test rig is presented.

Chapter 5: Accelerometer measurements of the physical system modeled in Chapter 4 are presented and interpreted. The signal processing methods used are described in detail. Eigenfrequencies are determined, and the corresponding mode shapes are estimated by a qualitative comparison of the accelerometer channels.

Chapter 6: The model described in Chapter 4 and the measurements from Chapter 5 are compared. It is shown that an accurate match between measurements and calculation can be established by using a model updating technique.

Chapter 7: Summarizes the contents of the report, and contains the main conclusions.

Chapter 2

Mesh Stiffness Modeling and Validation

In this chapter the mathematical model of the gear mesh stiffness will be described in detail. The main result is the gear mesh stiffness c, which is a function of the relative rotation of the meshing gears, applied load, gear data, and grinding corrections. The stiffness found will form the basis for the remaining part of the thesis.

The gear mesh stiffness is computed in a number of steps:

Initial geometric calculations: From basic input data, the involute profiles of the gear teeth can be determined. Data needed for the deformation and stiffness calculations are then found based on the tooth shape.

Tooth compliance matrix: For each relative gear position the theoretical position of the contact line across the tooth face can be found from simple trigonometric calculations. With this line a tooth compliance matrix based on flexibility influence coefficients can be set up. The tooth compliance matrices from the two mating teeth is combined to form a tooth pair compliance matrix. The Hertzian deformation, which is nonlinear, is not included in the compliance matrix, but enters the equations at a later stage.

Single tooth pair stiffness: In general the actual length of the contact line under load will not be equal to the length of the the theoretical

contact line, which was used as a basis for calculating the compliance matrix. To solve this contact problem, an iteration process is used to find the actual contact line and the load distribution across the tooth. The Hertzian deformation enters the equations at this stage. Also tooth grinding corrections are considered, as they greatly influence the load distribution and the length of the contact line. When these calculations have been performed, the position- and load-dependent single tooth pair deformation and stiffness are known.

Mesh stiffness: When the deformational behavior of a single tooth pair is known, the stiffness of the gear mesh, which usually includes more than one tooth pair in contact, can be found. Also the load sharing between the tooth pairs is found.

For helical gears, definitions of transverse and normal profiles are necessary. These are defined in DIN3998-1 [55] as shown in figure 2.1. For a spur gear

(a) Transverse profile   (b) Normal profile
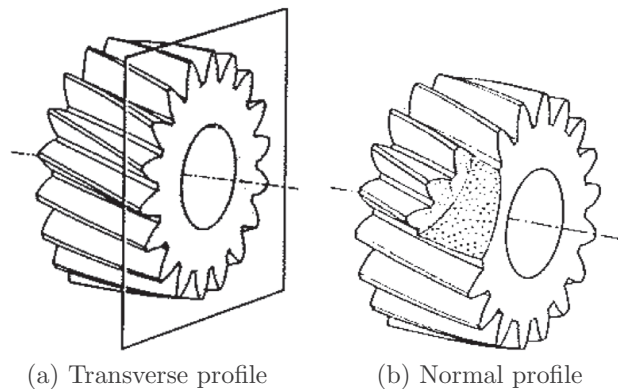
Figure 2.1: Transverse and normal tooth profiles. Figures from DIN3998-1 [55]

pair, the transverse and the normal profiles are identical.

2.1 Initial Geometric Calculations

Some basic input data for each of the two meshing gears is necessary for the calculations. The data needed is listed in table 2.1. Most of the symbols are standardized in DIN3999-1 [56], where also the English translations are

α_n	Normal pressure angle
β	Helix angle
z	Number of teeth
a	Centre distance
m_n	Normal module
x	Addendum modification coefficient
b	Face width
d_a	Tip diameter
d_f	Root diameter
h_{aP}	Addendum coefficient of basic rack
c	Tip clearance
h_{aP0}	Addendum coefficient of tool
ρ_{aP0}	Tip rounding radius of tool
pr_0	Amount of protuberance in tool
α_{pr0}	Protuberance angle
x_E	Generating addendum modification coefficient

Table 2.1: Gear input data

found. Further information can be found in DIN3960 [57].

With the presented input data, the involute transverse profile of the gear tooth η_S, as a function of the distance to the tooth tip ξ, can be calculated using the formulas presented by Padieth [58]. An example transverse profile is shown in figure 2.2(a). The normal tooth profile η is then calculated from the transverse profile as proposed by Ziegler [3], page 10:

$$r_p(\xi) = \sqrt{\eta_S(\xi)^2 + (r_a - \xi)^2} \qquad (2.1)$$

$$\beta_p(\xi) = \arctan(\frac{r_p(\xi)}{r}\tan\beta) \qquad (2.2)$$

$$\eta(\xi) = \eta_S(\xi)\cos\beta_p(\xi) \qquad (2.3)$$

From equations (2.1) through (2.3) it can be seen that the transverse and the normal profile are identical for a spur gear with $\beta = 0$. A normal profile is shown in figure 2.2(b). An axis ζ_S is also seen in figure 2.2(a) to complete the right-hand coordinate system $\eta_S\xi\zeta_S$. The ζ-axis is defined in a similar manner in the normal section.
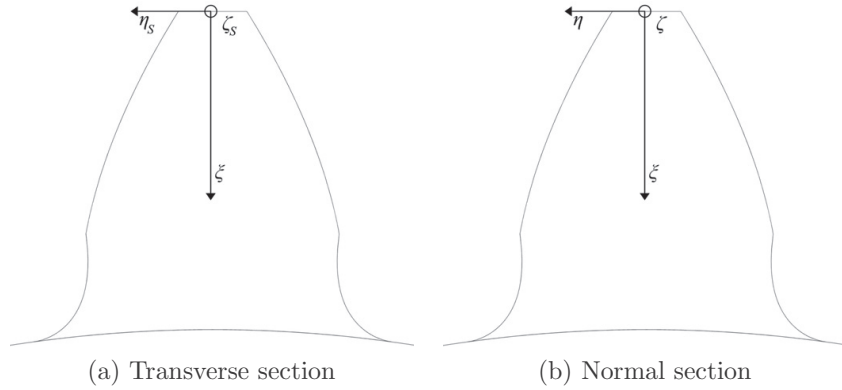
(a) Transverse section   (b) Normal section

Figure 2.2: Tooth profiles. The relation between the coordinate frames η, ξ, ζ and η_S, ξ_S, ζ_S can be seen in figure 2.1

To construct a tooth compliance matrix of finite dimension, a discretization of the tooth is necessary. This corresponds to laying out a grid over the tooth, as seen in figure 2.3. The grid consists of K_{MAX} lines in the ξ-direction, and I_{MAX} lines in the ζ-direction.

Now the tooth has been appropriately discretized, a number of properties related the tooth elasticity can be derived and related to the K-lines of the grid. For each index K in the interval $[1, K_{\text{MAX}}]$, the relevant parameters are: The profile coordinates $\xi(K)$, $\eta(K)$, and $\eta_S(K)$, the tooth thickness $H(K)$, the angle of attack $\alpha_{at}(K)$, and the bending moment of inertia $I_A(K)$:

$$H(K) \;=\; 2 \cdot \eta(K) \tag{2.4}$$

$$\alpha_{at}(K) \;=\; \arctan\left(\frac{\eta(K+1) - \eta(K)}{\xi(K+1) - \xi(K)}\right) \tag{2.5}$$

$$I_A(K) \;=\; \frac{2}{3}B\Big(\eta(K)\Big)^3 \tag{2.6}$$

In the formulas above, B is the tooth width in the normal direction, which is calculated from the transverse tooth width b using the formula $B = b\cos(\beta)$. Note that all properties are calculated in the normal section of the tooth, as the deformation calculations will be performed in the normal plane.
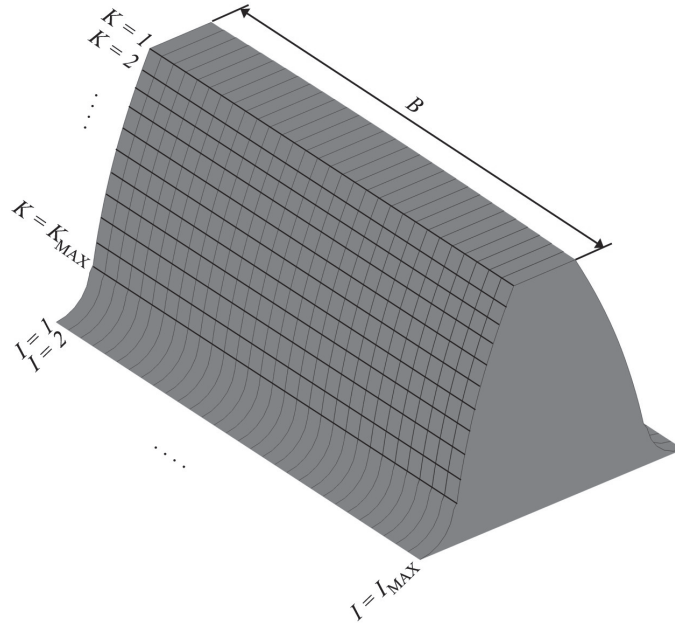
Figure 2.3: Tooth calculation grid

2.2 Tooth Compliance Matrix

The tooth compliance matrix will be constructed as a matrix of compliance influence coefficients (see [59, page 285ff]). The principle is to apply a unit force at a fixed point, and calculate the deflection of all points in the structure. The calculation is then repeated, but with a unit force applied at a different point.

If the system to be analyzed has N points, or degrees of freedom (DOF), the deflections and the external forces applied to the system can be set up in two $N \times 1$ vectors called $\mathbf{X}$ and $\mathbf{F}$, respectively, while the compliance matrix $\mathbf{Z}$ is of dimension $N \times N$:

$$\mathbf{X} = \mathbf{ZF} \tag{2.7}$$

If $\mathbf{F} = [1\ 0\ 0\ 0\ \ldots\ 0]^T$ the first column of $\mathbf{Z}$ will be identical with $\mathbf{X}$. For $\mathbf{F} = [0\ 1\ 0\ 0\ \ldots\ 0]^T$ the second column of $\mathbf{Z}$ will be identical with $\mathbf{X}$, and so on.

In this model, only deformations in the normal plane, in the direction of the line of action (LOA) are included. The LOA is shown schematically as the line AE in figure 2.4. With the tooth calculation grid described, this
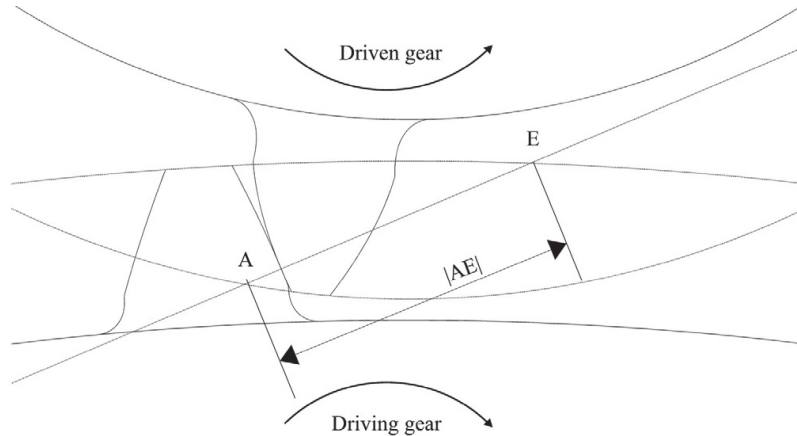

Figure 2.4: Zoom of the meshing teeth

means that the total number of DOFs is $N = K_{\mathrm{MAX}} \cdot I_{\mathrm{MAX}}$, and $\mathbf{Z}$ will be of dimension $(K_{\mathrm{MAX}} \cdot I_{\mathrm{MAX}}) \times (K_{\mathrm{MAX}} \cdot I_{\mathrm{MAX}})$.

The calculation of $\mathbf{Z}$ is simplified according to the assumption proposed by Schmidt [60]: The two directions of the tooth surface grid, the K and the I directions, can be treated separately, and submatrices $\mathbf{Z}_K$ and $\mathbf{Z}_I$ are found. These submatrices can be combined to form $\mathbf{Z}$.

First, the K-direction is considered. The problem can be described as *find the deflection of all sections K, resulting from an applied unit force at section K_P*. Since the problem is now one-dimensional, elements from elementary beam theory can be used, see figure 2.5. The derivation of $\mathbf{Z}_K$ follows the methods of Ziegler [3]. The total deformation of the tooth is a sum of several contributions (as mentioned earlier, the Hertzian deformation is not included in the compliance matrix):
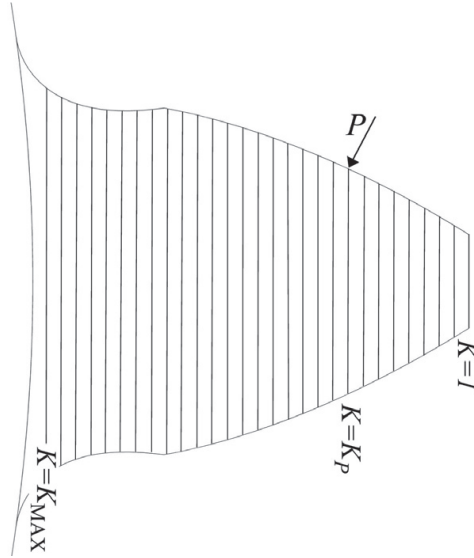
Figure 2.5: Tooth as discretized beam

$Y_{BE}(K)$	Bending
$Y_{SchE}(K)$	Shear
$Y_{RE}(K)$	Compression
$Y_{KE}(K)$	Gear body deformation

Using this notation, the total single tooth deformation at section K can be written as

$$Y_E(K) = Y_{BE}(K) + Y_{SchE}(K) + Y_{RE}(K) + Y_{KE}(K) \qquad (2.8)$$

In the following paragraphs, the derivation of the deformation components in equation (2.8) are described. It is shown that all deformations depend linearly on the load. The unit force P acts at section K_P, which is located at the coordinate $\xi = \xi_P$.

Bending deformation Y_{BE} The basic assumptions of the Bernoulli-Euler beam theory states that a plane cross section of an undeformed beam stays plane and perpendicular to the beam centreline during deformation. These assumptions are good approximations when the beam is long and slender. In the case of a short, gear-tooth shaped beam, the assumptions are not met.

However, it is common practice to estimate gear tooth stresses based on this theory. Therefore, the calculation of the gear tooth bending deformation in this work is based on Bernoulli-Euler beam theory. The tooth and the beam used for the calculations are shown in figure 2.6. The deflection of the beam
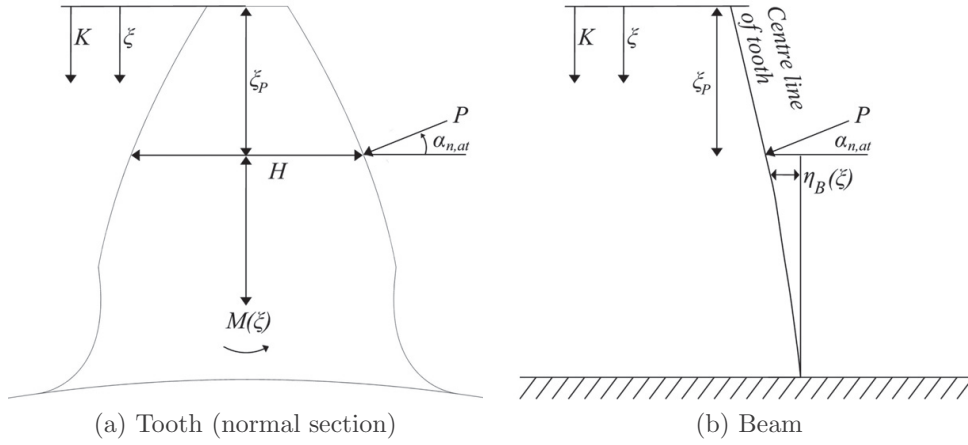

(a) Tooth (normal section) (b) Beam

Figure 2.6: The tooth and its beam equivalent

in the η-direction and normal to the undeformed beam centreline is called η_B. The beam will bend as a function of the bending moment. The bending moment is:

$$M(\xi) = \begin{cases} 0 & \text{for } \xi \leq \xi_P \\ -P\cos(\alpha_{n,at})(\xi - \xi_P) + P\frac{H}{2}\sin(\alpha_{n,at}) & \text{for } \xi > \xi_P \end{cases} \quad (2.9)$$

From beam theory, the curvature of the beam with Young's modulus E can be expressed as:

$$\frac{\mathrm{d}^2\eta_B}{\mathrm{d}\xi^2} = -\frac{M(\xi)}{I_A(\xi)E} \quad (2.10)$$

The deflection η_B is obtained by integrating twice in equation (2.10):

$$\eta_B(\xi_0) = -\int_0^{\xi_0}\int_0^{\xi_0} \frac{M(\xi)}{I_A(\xi)E} \, \mathrm{d}\xi \, \mathrm{d}\xi + C_1\xi_0 + C_2 \quad (2.11)$$

(In equation (2.11), the upper integration limit is temporarily called ξ_0). The integration constants C_1 and C_2 are found from the boundary conditions at

$\xi = L$ for the cantilever beam, where L is the total tooth depth:

$$\frac{\mathrm{d}\eta_B}{\mathrm{d}\xi}\bigg|_{\xi=L} = 0 \tag{2.12}$$

$$\eta_B(\xi = L) = 0 \tag{2.13}$$

Equation (2.11) yields the deflection $\eta_B(\xi)$ in the normal plane, normal to the centreline of the undeformed tooth, and for all values of ξ, as shown in figure 2.6(b). This deflection is then transformed into the transverse plane, in the direction of the line of action, with the formula

$$Y_{BE} = \eta_B \frac{\cos \alpha_{wt}}{\cos \beta} \tag{2.14}$$

Shear deformation Y_{SchE} The shear deformation in the tooth is caused by the force $P_S = P \cos(\alpha_n)$, as shown in figure 2.7. The shear stress is found

(a) Tooth (normal section) (b) Beam
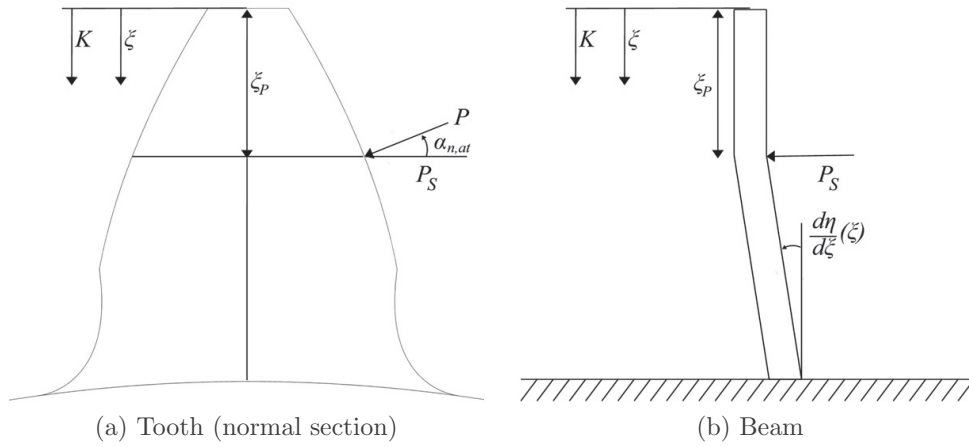
Figure 2.7: The tooth and its beam equivalent

by dividing P_S with the cross sectional area $2B\eta(\xi)$ below section K_P:

$$\tau(\xi) = \begin{cases} 0 & \text{for } \xi \leq \xi_P \\ \frac{P_S}{2B\eta(\xi)} & \text{for } \xi > \xi_P \end{cases} \tag{2.15}$$

As for the bending calculation, finding the shear deformation includes solving a differential equation. In equation (2.16), κ is the Timoshenko shear

coefficient. For a rectangular cross section, $\kappa = 5/6$. G is the shear modulus.

$$\frac{\mathrm{d}\eta_{Sch}}{\mathrm{d}\xi} = \frac{\tau(\xi)}{\kappa G} \Rightarrow \eta_{Sch}(\eta_0) = \frac{1}{\kappa G} \int_0^{\eta_0} \tau(\xi)\mathrm{d}\eta + C_3 \tag{2.16}$$

The upper integration limit is temporarily renamed. Using the boundary condition $\eta_{Sch}(\xi = L) = 0$, the integration constant C_3 in equation (2.16) is found. Again, the deformation is transformed using the equation

$$Y_{SchE} = \eta_{Sch} \cdot \frac{\cos \alpha_{wt}}{\cos \beta} \tag{2.17}$$

Compression Y_{RE} The radial force $P_R = P \sin(\alpha_n)$ will cause a small compressive deformation of the tooth, as shown in figure 2.8. Obviously, this
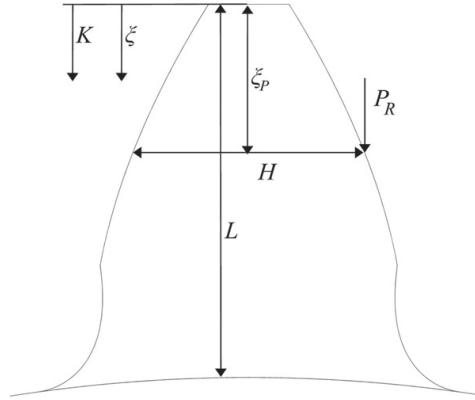
Figure 2.8: Compression of the tooth

type of deformation will only give a small contribution to the total tooth deformation. Therefore, a simplifying assumption is made: The tooth is assumed to have constant thickness $H(\xi_P)$ for all values of ξ. $H(\xi_P)$ is the correct tooth thickness at the contact point $\xi = \xi_P$. The compressive force P_R is evaluated at the contact point by using the pressure angle $\alpha_{n,at}$ evaluated at the contact point. This means, that the compression in the ξ-direction can be expressed as:

$$\xi_R(\xi) = \frac{P_R(L - \xi)}{H(\xi_P)BE_{eff}} \tag{2.18}$$

The compressive force will also lead to a deformation in the η-direction:

$$\eta_R(\xi) = \nu \xi_R(\xi) \tag{2.19}$$

In equation (2.19) ν is the Poisson ratio. Equations (2.18) and (2.19) can now be combined to give the deformation in the transverse plane, in the direction of the line of action:

$$Y_{RE} = \xi_R \tan(\alpha_n - \nu) \frac{\cos \alpha_n}{\cos \beta} \tag{2.20}$$

Gear body compliance Y_{KE} As opposed to the other deformation contributions, the gear tooth is in this section considered rigid and the gear body is assumed elastic, see figure 2.9. The distance in the ξ-direction from the
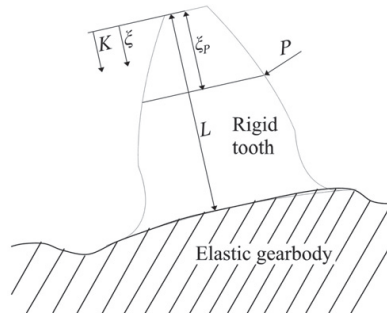
Figure 2.9: The rigid tooth and the elastic gear body

gear body to the point of contact is called $y_p = L - \xi_P$. As seen in figure 2.9, the deformation of the gear body, measured at the contact point in the direction of the line of action, can be split up into two components: Y_{KP} from the tooth translation, and Y_{KM} as a result of tooth rotation. Several authors give equations for the calculation of these quantities [2, 61]. The

method chosen here is from [2]. First, a few quantities must be defined:

$$H_{root} \quad : \quad \text{Thickness of tooth at the root, normal section} \qquad (2.21)$$

$$C_{11} \quad = \quad \frac{9(1 - \nu^2)}{E\pi B H_{root}^2} \qquad (2.22)$$

$$C_{12} \quad = \quad \frac{(1 + \nu)(1 - 2\nu)}{E\pi B H_{root}} \qquad (2.23)$$

$$C_{22} \quad = \quad \frac{2.4(1 - \nu^2)}{E\pi B} \qquad (2.24)$$

Now the deformations are found:

$$Y_{KP} \quad = \quad 2C_{22}P\cos^2\alpha_{n,at}\left(1 + 0.294\tan^2\alpha_{n,at}\right) \qquad (2.25)$$

$$Y_{KM} \quad = \quad 2P\cos^2\alpha_{n,at}\left(C_{11}y_p^2 + 2C_{12}y_p\right) \qquad (2.26)$$

$$Y_K \quad = \quad Y_{KP} + Y_{KM} \qquad (2.27)$$

$$Y_{KE} \quad = \quad Y_K\frac{1}{\cos\beta} \qquad (2.28)$$

It has now been shown, how the deflection at any coordinate ξ can be calculated when a unit force P is applied at the coordinate ξ_P. This is sufficient information to construct the compliance matrix $\mathbf{Z}_K$.

Plate influence coefficients In the previous section all slices across the tooth have been treated equally - this means that a force on slice no. 1 will cause identical deformations on slice no. 1 and slice no. n, for $n \in [1, I_{\text{MAX}}]$. This is only a good approximation for very narrow-faced gears. For wider gears, deformations will depend on the ζ-coordinate of the applied force. This means that the influence between neighboring slices must be altered to take this effect into account. One way of doing this is to include a simplified plate, as done by Schmidt [60], see figure 2.10. The idea is to regard a tooth as a plate, figure 2.10(a). The elastic deformation of the plate is approximated by an Euler-beam, which is elastically supported by both torsional and linear springs, figure 2.10(b). Now the problem of finding the influence between slices in the tooth reduces to finding the bending stiffness F of the beam and stiffnesses c_1 and c_2 of the support. With these constants found, the 4th order differential equation describing the beam bending f is derived:

$$F\frac{\mathrm{d}^4 f}{\mathrm{d}\zeta^4} - c_2\frac{\mathrm{d}^2 f}{\mathrm{d}\zeta^2} + c_1 f = P(\zeta_P) \qquad (2.29)$$

(a) Plate   (b) Simplified plate (beam)
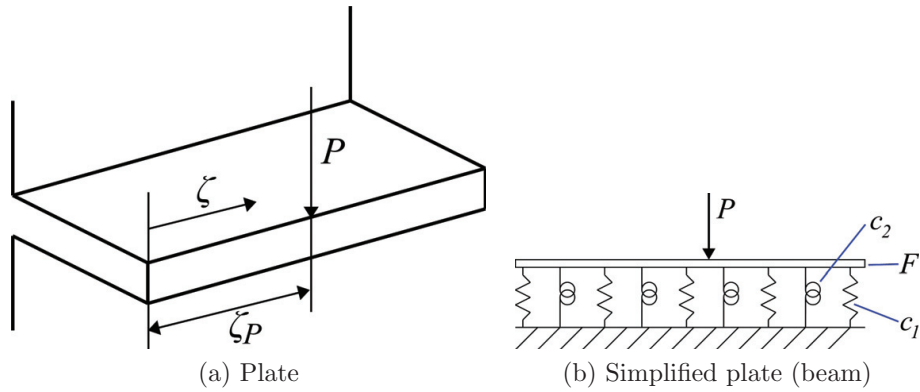
Figure 2.10: Simplified plate theory, according to [60]

This equation is solved using the magnitude and the position of the applied force, P and ζ_P, as boundary conditions. The calculations are repeated for several values of ζ_P, and the result is the matrix $\mathbf{Z}_I$. For a simple example system with $I_{\mathrm{MAX}} = 5$, the columns of $\mathbf{Z}_I$ have been plotted in figure 2.11. The highlighted line is the $\mathbf{Z}_I$-column for which the force is applied at the left
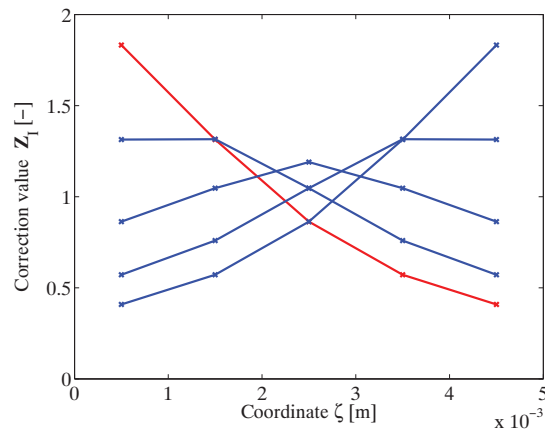
Figure 2.11: $\mathbf{Z}_I(\zeta_P, \zeta)$

edge of the tooth, $\zeta_P = 0$. The $\mathbf{Z}_I$-columns are normalized to give an average value of 1. This makes $\mathbf{Z}_I(\zeta_P, \zeta)$ a suitable correction function, which can be multiplied by the compliances in $\mathbf{Z}_K$ to give a realistic displacement pattern

Page 34 of 139

across the tooth.

With $\mathbf{Z}_K$ and $\mathbf{Z}_I$ found, all necessary information to assemble the $(K_{\text{MAX}} \cdot I_{\text{MAX}}) \times (K_{\text{MAX}} \cdot I_{\text{MAX}})$ tooth compliance matrix $\mathbf{Z}$ is available. However, to ensure sufficient accuracy of the results, both K_{MAX} and I_{MAX} need to be relatively large, which leads to an unreasonably large $\mathbf{Z}$. For a given relative gear position, the mating teeth will touch at a line across the tooth surface. The position and orientation of this contact line depends on the gear positions and on the helix angle. In figure 2.12, the contact line is shown for a helical gear pair. Without loss of accuracy, this line can be discretized into
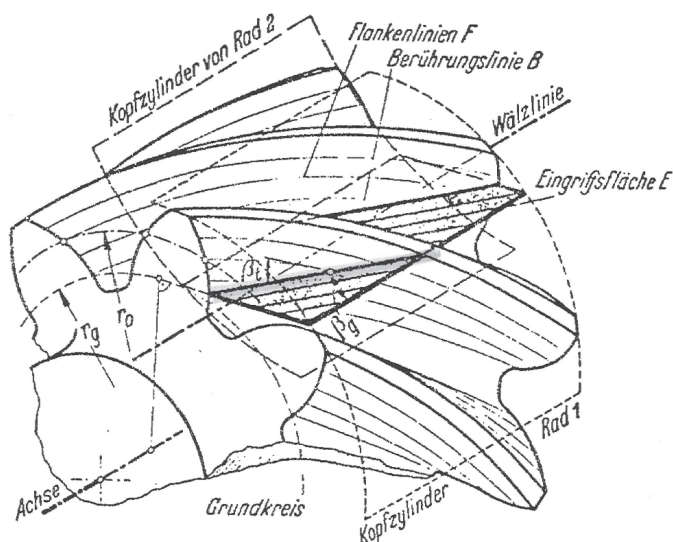

Figure 2.12: Position of contact line, helical gear, figure from [60]

a number of points. From figure 2.13, where the contact line is shown for two meshing positions, it is clear that no more than one section K of each slice I will touch the mating gear. Since only the contacting sections K and slices I are of any interest, the remaining sections and slices can be discarded. This leads to a maximum dimension $(I_{\text{MAX}} \times I_{\text{MAX}})$ of $\mathbf{Z}$. However, since the position of the contact line depends on the relative gear position, $\mathbf{Z}$ needs to be renewed for each new gear position.

For a given slice I, the meshing is shown in figure 2.4. It is apparent that the
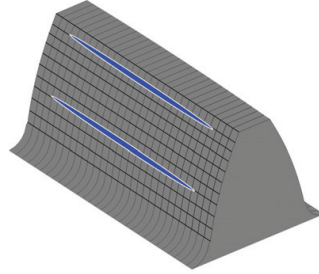
Figure 2.13: Position of contact line on the calculation grid, spur gear

contact point on the ξ-axis in the tooth coordinate system will always lie in the interval $[0, r_a - \text{SAP}]$. Now the line AE is simply divided into $J_{\text{MAX}} - 1$ pieces of equal length, which corresponds to J_{MAX} equally spaced relative gear mesh positions. For any position J, the ξ-coordinate of the contact point, ξ_P, on the driving gear (gear 1) is found by using the formula:

$$\xi_{P,J} = (r_{a,1} - \text{SAP}_1) - \frac{J-1}{J_{\text{MAX}} - 1} \cdot (r_{a,1} - \text{SAP}_1) \tag{2.30}$$

Likewise, for the driven gear (gear 2) the contact point is found as

$$\xi_{P,J} = \frac{J-1}{J_{\text{MAX}} - 1} \cdot (r_{a,2} - \text{SAP}_2) \tag{2.31}$$

Now for each position J and for each slice I a nearest-point interpolation is performed to find the section K closest to the theoretical contact point at ξ_P. In this way the position of the theoretical contact line across a tooth on the driving gear for a given mesh position J can be described by a vector of dimension I_{MAX} called $\mathbf{K}_{1,J}$, which contains the index numbers K of the contacting sections. Likewise, a vector $\mathbf{K}_{2,J}$ describes the theoretical contact line for a tooth on the driven gear.

For a helical gear, the contact line will often be shorter than the distance across the tooth, see figure 2.13. In this case, the vectors $\mathbf{K}_{1,J}$ and $\mathbf{K}_{2,J}$ will simply be of smaller dimension.

Consider the relative gear mesh position J. In this position, the tooth compliance matrix $\mathbf{Z}_{1,J}$ for gear 1 is ready to be assembled using the matrices

$\mathbf{Z}_I$ and $\mathbf{Z}_K$, and the vector $\mathbf{K}_{1,J}$. Assume that $\mathbf{K}_{1,J}$ has the length I_L. Then $\mathbf{Z}_{1,J}$ will be of dimension $I_L \times I_L$, and can be populated in a simple manner:

$$\mathbf{Z}_{1,J}(I_A, I_B) = \mathbf{Z}_K\Big(\mathbf{K}_{1,J}(I_A), \mathbf{K}_{1,J}(I_B)\Big) \cdot \mathbf{Z}_I(I_A, I_B) \qquad (2.32)$$

$$\text{for } I_A = 1\dots I_L \text{ and } I_B = 1\dots I_L \qquad (2.33)$$

In a similar way, the tooth compliance matrix $\mathbf{Z}_{2,J}$ for gear 2 can be assembled. Now the two single-tooth compliance matrices are added to produce the tooth pair compliance matrix for position step J:

$$\mathbf{Z}_J = \mathbf{Z}_{1,J} + \mathbf{Z}_{2,J} \qquad (2.34)$$

Grinding corrections   To ensure smooth running of the gears, small amounts of material are often removed from the tooth surfaces. This can be done in many ways, examples are shown in figure 2.14. Often modifications are expressed by a power law.

Profile modifications are defined along the line of action (LOA), the line AE in figure 2.4. For a tip modification, the amount of material removed (in the direction of the LOA) at any coordinate s along the LOA, $y(s)$, is described by the amount removed at the tooth tip C_a, the length of the modification L_a, and an exponent n to describe the shape of the modification. The equation is

$$y(s) = C_a\left(\frac{L_a - s}{L_a}\right)^n \text{ for } s \in [0, L_a] \qquad (2.35)$$

with $s = $ distance from point E on the LOA for gear 1, and $s = $ distance from point A on the LOA for gear 2. For root relief, a similar equation can be set up. The index f is used for root modifications. For a profile crowning, the symbol C_h is used. Profile crowning can be seen as a combination of a long tip and a long root relief.

Lead modifications are defined across the tooth width. For end relief, the amount C_e, the length b_e, and the shape exponent m can be defined for both ends of the tooth. When t is the distance to the tooth end, the end relief follows the equation

$$y(t) = C_e\left(\frac{b_e - t}{b_e}\right)^m \text{ for } t \in [0, b_e] \qquad (2.36)$$
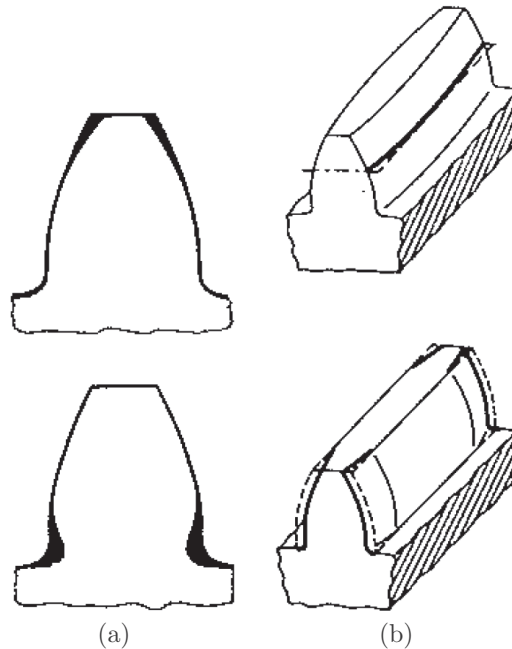
Figure 2.14: Examples of grinding corrections, figure from [55]. (a) Profile modifications: Tip relief and root relief. (b) Lead modifications: Crowning and end relief

An extra index R or L can be used to indicate right or left tooth end. For a lead crowning, the symbol C_b is used. Lead crowning corresponds to a double-sided end relief, with $C_{eR} = C_{eL} = C_b$ and $b_{eR} = b_{eL} = B/2$, where B is the tooth width. In figure 2.15, example tip relief ($C_a = 60$ μm, $L_a = 15$ mm, $n = 2$) and lead crowning ($C_b = 20$ μm, $m = 2$) are shown. These values for m and n are typical values used in industrial applications, and therefore both m and n are set to 2 in this work. The sum of the grinding corrections applied to a tooth is put into a ($I_{\text{MAX}} \times K_{\text{MAX}}$) matrix meaning that the amount of material removed from each point of the grid is known, see figure 2.16. Now the vectors $\mathbf{K}_{1,J}$ and $\mathbf{K}_{2,J}$ can be used to find the grinding corrections at all points on the theoretical contact line. This results in a vector $\mathbf{d}_J$, which will be used in the following calculations.
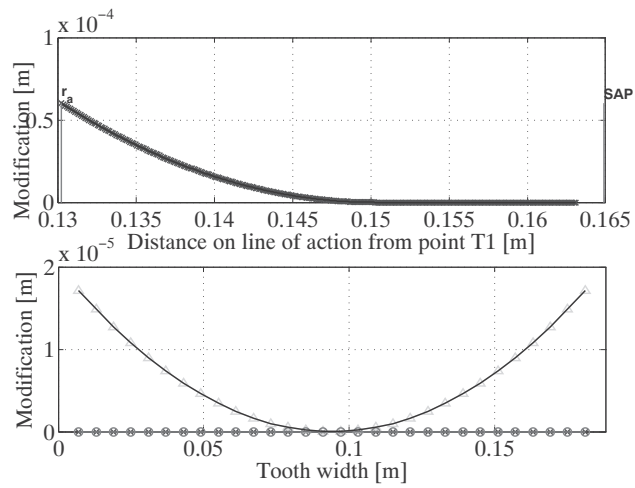
Figure 2.15: Material removed by grinding corrections, profile (top) and lead (bottom) directions
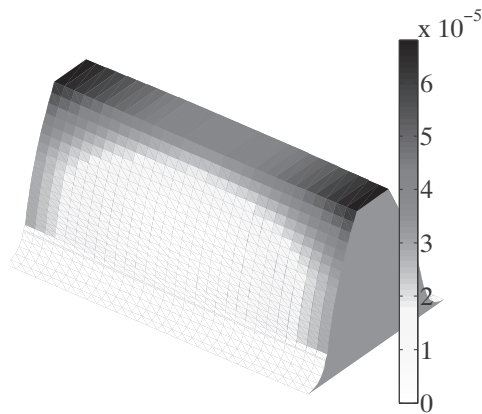

Figure 2.16: Material removed [m] from the tooth flanks by grinding corrections, 3D view

2.3 Single Tooth Pair Stiffness

The Hertzian (or contact) deformation differs from the other types of deformation considered here, as it depends on both of the contacting teeth. It is the only deformation component to vary nonlinearly with the applied load. The calculation procedure presented here is very close to the procedures presented by Ziegler [3] and Weber and Banaschek [2].

The Hertzian deformation depends on the radii of curvature of the contacting surfaces, ρ_1 and ρ_2, which can be found as shown in figure 2.17. From the
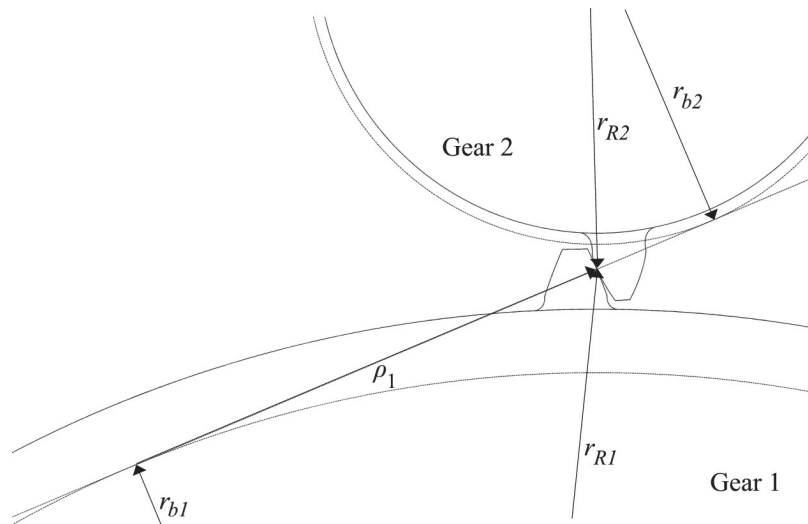

Figure 2.17: Calculation of the radius of curvature for a section I

figure it is seen that the radii of curvature can be calculated as

$$\rho_1 = \sqrt{r_{R1}^2 - r_{b1}^2}\,\frac{1}{\cos\beta_b} \tag{2.37}$$

$$\rho_2 = \sqrt{r_{R2}^2 - r_{b2}^2}\,\frac{1}{\cos\beta_b} \tag{2.38}$$

The factor $1/\cos(\beta_b)$ in the above equations transforms ρ_1 and ρ_2 from the transverse to the normal plane. Equations (2.37) and (2.38) can be rewritten in a single equation for the calculation of a combined radius of curvature

taking into account both gears:

$$\rho = \frac{\rho_1 \rho_2}{\rho_1 + \rho_2} \tag{2.39}$$

Now a few quantities can be defined[1]:

$$
\begin{aligned}
W_0 &= \frac{P_{BE}(I)}{B/I_{\text{MAX}}} & \text{Line load} & \tag{2.40} \\
p_{max} &= \sqrt{\frac{W_0 E}{2\pi\rho(1-\nu^2)}} & \text{Maximum Hertzian pressure} & \tag{2.41} \\
b &= \sqrt{\frac{8 W_0 \rho(1-\nu^2)}{E\pi}} & \text{Half width of zone of influence} & \tag{2.42} \\
h &= \frac{H}{2\cos\alpha_n} & \text{Depth of zone of influence} & \tag{2.43}
\end{aligned}
$$

The value of h in equation (2.43) is chosen rather arbitrarily as the distance from the contact point to the tooth centreline, see figure 2.18, as this seems to be a good approximation. From Weber and Banaschek [2], the Hertzian
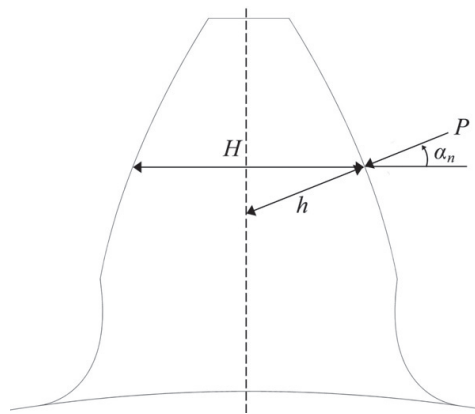

Figure 2.18: Definition of the "depth of zone of influence", h (normal plane)

deformation in the normal plane in the direction of the line of action is now

---

[1]The maximum Hertzian pressure p_{max} is not used here, but it is needed at a later stage

given as

$$Y_A = \frac{2W_0(1-\nu^2)}{E\pi}\left(\ln\left(\frac{2h}{b}\right) - \frac{\nu}{2(1-\nu)}\right) \qquad (2.44)$$

Again, to transform from normal to transverse plane:

$$Y_{AE} = Y_A\frac{1}{\cos\beta} \qquad (2.45)$$

To use the compliance matrix $\mathbf{Z}$ as shown in equation (2.7), the load distribution $\mathbf{F}$ across the tooth must be known. Because of elastic deformation in the gear teeth, and because of the applied tooth modifications, the actual contact line may not be identical to the theoretical contact line determined in a previous section. For these reasons, a contact model must be set up. The model shown in figure 2.19 can be used. In the figure, a spring represents the elasticity associated with a slice I of the contact line. The tooth elasticity $\mathbf{Z}$ is shown as a number of springs enclosed in a rectangular box to illustrate the interactions between the springs. Mathematically this corresponds to the general case, where $\mathbf{Z}$ is a full matrix and not a diagonal matrix. $\mathbf{Z_H}$ represents the Hertzian deflection, which is a localized deformation type with no influence between neighboring slices. Because of the modifications, the teeth
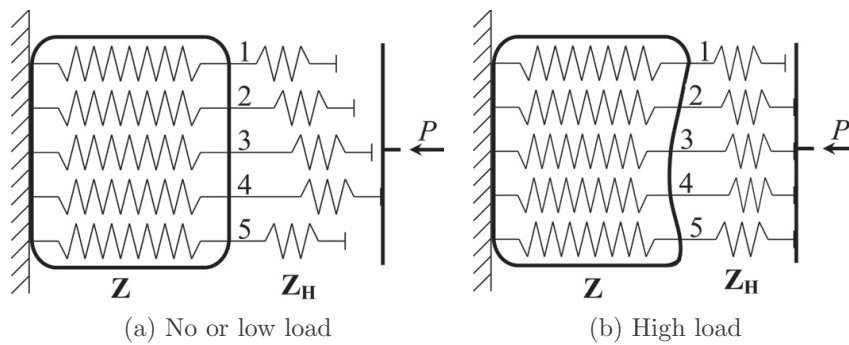

(a) No or low load   (b) High load

Figure 2.19: Tooth stiffness model

may only touch at one point at low load, as shown in figure 2.19(a). When the load increases, more slices I enter into contact, see figure 2.19(b). At

low load, when only some springs are in contact, the tooth pair stiffness will therefore have two different built-in nonlinearities with respect to the load P: 1) The Hertzian deformation is nonlinear in P, and 2) The length of the contact line increases with increasing load. To solve this nonlinear problem, an iterative procedure is chosen. For a fixed load P, the calculations follow the scheme below, which consists of two nested loops: The purpose of the outer loop is to determine which slices are in contact, and the inner loop finds the correct load distribution $\mathbf{F}$. In order to find $\mathbf{F}$, the assumption is made that all contacting slices deflect the same amount, when including modifications as a deflection. The same assumption is made by Ziegler [3].

1. To initialize the force vector $\mathbf{F}$, all load P is put on the slice I, which shows the smallest amount of modification $\mathbf{d}$ (in figure 2.19, this is slice 4)

   (a) For the current load distribution $\mathbf{F}$, the Hertzian deformation $\mathbf{X}_H$ is calculated (for unloaded slices, $X_H = 0$)

   (b) The tooth deformation $\mathbf{X}_T$ is calculated

   (c) The displacement $\mathbf{Y} = \mathbf{X}_H + \mathbf{X}_T + \mathbf{d}$ is calculated.

   (d) The "displacement ratio" vector $\mathbf{Y}_{\text{ratio}} = \mathbf{Y}/\text{mean}(\mathbf{Y})$ is calculated for the *loaded* slices only

   (e) The load distribution $\mathbf{F}$ is updated using the formula $\mathbf{F}_{\text{new}} = \left(\frac{1}{\mathbf{Y}_{\text{ratio}}}\right)\mathbf{F}_{\text{old}}$ to increase the load on the slices I that are less-than-average deflected

   (f) The vector $\mathbf{F}$ is scaled to ensure $\sum \mathbf{F} = P$

   (g) If the largest component of $\mathbf{Y}_{\text{ratio}}$ is still above a pre-set limit, return to step 1a. Otherwise, the loop is ended

2. The "overall elastic tooth pair deformation" $X = \max(\mathbf{X}_H + \mathbf{X}_T)$ is saved

3. For a given *unloaded* slice I, the elastic deformation required to be in contact is $\mathbf{d}(I) + \mathbf{X}_T(I)$. If $X > \mathbf{Y}(I)$, slice I must carry load. In this case update $\mathbf{F}$ so that $\mathbf{F}(I) > 0$, scale $\mathbf{F}$ to ensure $\sum \mathbf{F} = P$ and return to step 1a. Otherwise, the loop is ended

The calculations described here are repeated for several loads P and several relative gear positions τ. The resulting deformation function $X(P, \tau)$ is stored as two piecewise linear functions $X(P)$ and $X(\tau)$ to be used in the gear mesh computations.

The single tooth pair stiffness c_E can be calculated using one of the two following definitions:

$$c_{E,\text{tangent}} = \frac{\mathrm{d}P}{\mathrm{d}X} \quad \text{Tangent stiffness} \tag{2.46}$$

$$c_{E,\text{secant}} = \frac{P}{X} \quad \text{Secant stiffness} \tag{2.47}$$

2.4 Gear Mesh Stiffness

The load- and position-dependent deflections for several single tooth pairs can be combined to a mesh deflection Y and a mesh stiffness c. The method used here is closely related to the method described by Gregory, Harris and Munro [13], but generalized to high-contact ratio gear sets with $\epsilon_\gamma > 2$.

Again, the grinding corrections are an important aspect of the calculations. In figure 2.20, the effective modifications along the line of action are shown for five tooth pairs. The number of tooth pairs in contact at a point on the LOA depends on the deformation of the gear mesh, and hence on the load. At a fixed relative gear position τ, consider three different loads marked 1, 2, and 3 in the figure. At low load (point 1) only one tooth pair is in contact. With increasing load, the gear mesh deformation increases. When this deformation increases above the amount of modifications of a tooth pair, the tooth pair will start carrying load. The modification of tooth pair n is called X_n. This is shown by the points 2 and 3 in figure 2.20, where two and three tooth pairs are in contact, respectively. Since the position- and load-dependent deformation behavior of a single tooth pair is known, the load sharing between the tooth pairs, the deformation of each tooth pair, and the total gear mesh deflection can be found. From this deflection, the gear mesh stiffness is found using formulas similar to equation (2.46) or (2.47).

For a given relative gear position τ, the computational procedure is explained using figure 2.21. This situation corresponds to the "high load" situation in
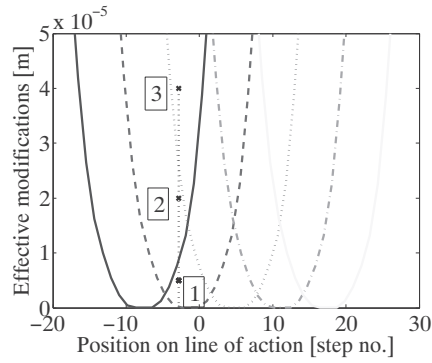
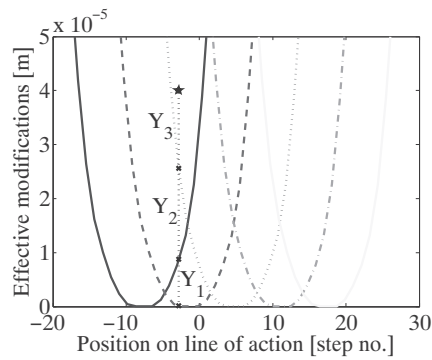Figure 2.20: Increasing number of load carrying tooth pairs with increasing load

Figure 2.21: Calculation procedure

figure 2.20, where three tooth pairs (TPs) share the load. But to explain the physics, let the gear mesh load P increase slowly from zero.

At the current τ, TP2 is the first TP to enter contact, when the load increases. This happens roughly at $Y = 0$, which means that the no-load transmission error X_0 is close to zero. When TP2 has deformed an amount Y_1, TP1 enters into contact. When the load increases further, also TP3 will enter into contact. This means that in the situation shown, TP3 is deformed the amount Y_3, TP1 is deformed $Y_3 + Y_2$, and TP2 is deformed $Y_3 + Y_2 + Y_1$. The total gear mesh deflection is defined as $Y_3 + Y_2 + Y_1$,

equal to the most deformed single TP. The governing equations to find the six unknowns $(P_1, P_2, P_3, Y_1, Y_2, Y_3)$ are

$$
\begin{aligned}
Y_3 &= Y(P_3, \tau_3) & (2.48) \\
Y_2 + Y_3 &= Y(P_2, \tau_2) & (2.49) \\
Y_1 + Y_2 + Y_3 &= Y(P_1, \tau_1) & (2.50) \\
Y_1 &= X_1 - X_0 & (2.51) \\
Y_2 &= X_2 - X_1 & (2.52) \\
P &= P_1 + P_2 + P_3 & (2.53)
\end{aligned}
$$

However, it is not enough to simply solve these six equations, as the number of TPs in contact is not known from the start. Again, an iteration loop is needed.

The total contact ratio ϵ_γ shows the average number of TPs in contact. Therefore ϵ_γ rounded up to the nearest integer can be seen as the maximum number of contacting TPs, that is possible at any time. In special cases however, a high load may increase the actual number of TPs in contact by one. This number, ϵ_γ rounded up plus one, is called N_{max}.

Initially, it is assumed that N_{max} TPs share the load P equally with $P_i = P/N_{\text{max}}$ for $i = 1 \ldots N_{\text{max}}$. Equations (2.48) through (2.53) are solved to give forces P_i and deformations Y_i. This is done in an iteration loop because of the nonlinear nature of the function $Y(P)$. If, during these calculations, a force P_i falls below a predefined limit, the corresponding TP is left out of the remaining calculations.

The procedure is repeated for several positions on the LOA. Now the gear mesh deflection is known, and the gear mesh stiffness can be found:

$$
\begin{aligned}
c_{\text{tangent}} &= \frac{\mathrm{d}P}{\mathrm{d}Y} \quad \text{Tangent stiffness} & (2.54) \\
c_{\text{secant}} &= \frac{P}{Y} \quad \text{Secant stiffness} & (2.55)
\end{aligned}
$$

The described calculation procedure for finding the gear mesh stiffness can be used for both external and internal gear meshes. The internal mesh is found in a planetary gear train, which is present in most modern wind turbine gearboxes.

The above discussion shows how the transmission error (TE) is closely linked to both modifications, stiffness, and loading of the gear teeth. In the proposed mesh stiffness model, the concept of TE is therefore included; however, it is regarded as a result of externally applied load and gear geometry and not treated as a excitation source.

2.5 Validation of Mesh Stiffness Model

In this section, the proposed gear stiffness model will be validated. This is done by comparing tooth deflection and stiffness to both experimental and model results from the literature.

In ISO-6336 [7], the maximum single tooth pair stiffness c' and the mean gear mesh stiffness c_γ are defined. Also methods and parameter values for the calculation are available. Therefore the mentioned ISO standard could be used for validation of c' and c_γ. However, c' and c_γ are scalar values and give no information on the influence of the relative gear position on the tooth and gear mesh stiffnesses. Since this dependency is essential for the work presented in this thesis, alternative data sources for the stiffness validation have been used.

The gear mesh stiffness is validated by comparison with the commercial software KissSoft[2]. Several gear pairs will be used in the validation process, to obtain results comparable to those reported in the literature. The gear pair chosen for the mesh stiffness validation is used in the following time-varying modal analysis.

Single tooth and tooth pair deflection First, single tooth deflections for a spur gear pair from Weber and Banaschek [2] are used for comparison. The gear pair is described in table 2.2. In [2], a rack with $z \to \infty$ is used as

|	Gear 1	Gear 2	Description	Unit
z	∞	24	Number of teeth	-
x	0	0	Addendum modification coefficient	-
b	5	5	Tooth width	mm
ρ_f	$0.39 \cdot m_n$	$0.39 \cdot m_n$	Root fillet radius	mm
m_n	1		Normal module	mm
α_n	20		Normal pressure angle	deg
β	0		Helix angle	deg
a	262		Centre distance	mm

Table 2.2: Data for spur gear pair used by Weber and Banaschek

---

[2]http://www.kisssoft.ch/english/products/kisssoft_gear.php

driving gear. However, in the model proposed here, $z \to \infty$ causes numerical problems, and the rack is replaced by a very large gear with $z = 500$. Weber and Banaschek present results for three combinations of gears, and for two loads per gear pair. The results are given as normalized deflection $q = \frac{yBE}{P}$, where y is the deflection, B is the tooth width, E is Young's modulus, and P is the load. Single tooth deflections are q_1 and q_2, and the Hertzian deflection is q_H. The results are presented in figure 2.22. It can be concluded that there is a good agreement between the deflections calculated by the two models.
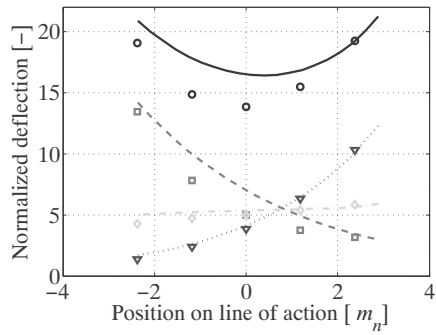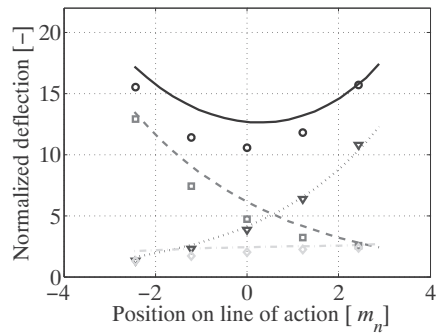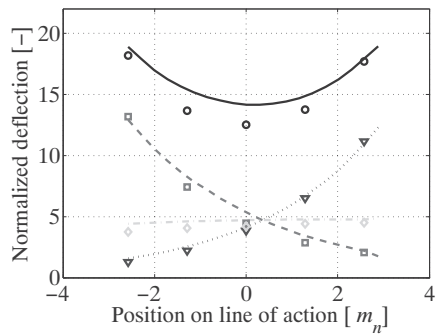
(a) $z_2 = 24$, $p_{max} = 2000$ kg/cm^2
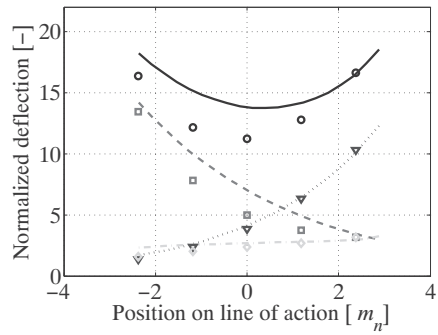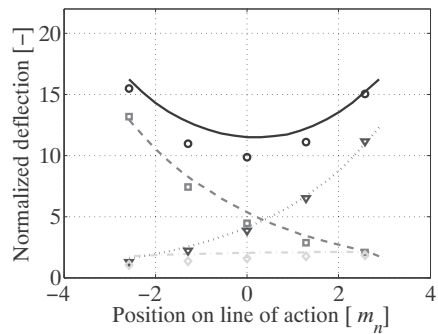
(b) $z_2 = 24$, $p_{max} = 20000$ kg/cm^2
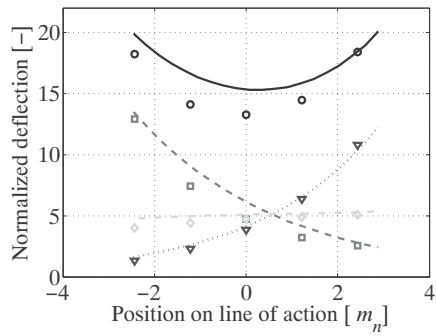
(c) $z_2 = 32$, $p_{max} = 2000$ kg/cm^2

(d) $z_2 = 32$, $p_{max} = 20000$ kg/cm^2

(e) $z_2 = 48$, $p_{max} = 2000$ kg/cm^2

(f) $z_2 = 48$, $p_{max} = 20000$ kg/cm^2

Figure 2.22: Tooth pair compliance compared to Weber and Banaschek. The markers represent Weber and Banaschek's values, and the lines show the results from the present model: ——○ q; $\cdots\triangledown$ q_1; ---□ q_2; $-\cdot-\diamond$ q_H

Tooth pair deflection In [6], Arafa and Megahed compute single-tooth compliance and tooth-pair compliance for two different gear sets. A finite element model of two meshing gears is used. The results are presented as normalized compliance $NC = \delta f / F_n$, or $NC = Yb/P$ with the notation used in this work. The data for the two gear pairs are shown in table 2.3. As

	Gear 1	Gear 2	Unit		Gear 1	Gear 2	Unit
z	20	20	-	z	70	70	-
x	0	0	-	x	0	0	-
b	5	5	mm	b	5	5	mm
ρ_f	$0.30 \cdot m_n$	$0.30 \cdot m_n$	mm	ρ_f	$0.30 \cdot m_n$	$0.30 \cdot m_n$	mm
m_n	2		mm	m_n	2		mm
α_n	20		deg	α_n	20		deg
β	0		deg	β	0		deg
a	40		mm	a	140		mm

(a) Gear pair 1   (b) Gear pair 2

Table 2.3: Data for gear pairs used by Arafa and Megahed

seen from the table, the two gear pairs consist of identical gears. The tooth pair compliance calculated by Arafa and Megahed compared to the present model is presented in figure 2.23. It must be noted that the finite element model proposed in [6] does not include the Hertzian deformation as a separate deflection component. Instead, the elements are very small to include the localized contact deformation. Therefore care must be taken when comparing to the present model, where the Hertzian deflection is *not* included in NC_1 and NC_2. Because of this difference in computational procedure, the single-tooth deflections are not expected to be identical, but the tooth pair deflections are directly comparable.

In figure 2.23(a), the single-tooth compliance and tooth-pair compliance is shown for the 20/20 gear pair. It is seen how the single tooth compliance curves for the two models differ at contact near the tooth root (the low compliance area). In this zone, the model presented here shows a compliance lower than Arafa and Megahed's model. The difference seems to decrease, as the contact point moves up the tooth.
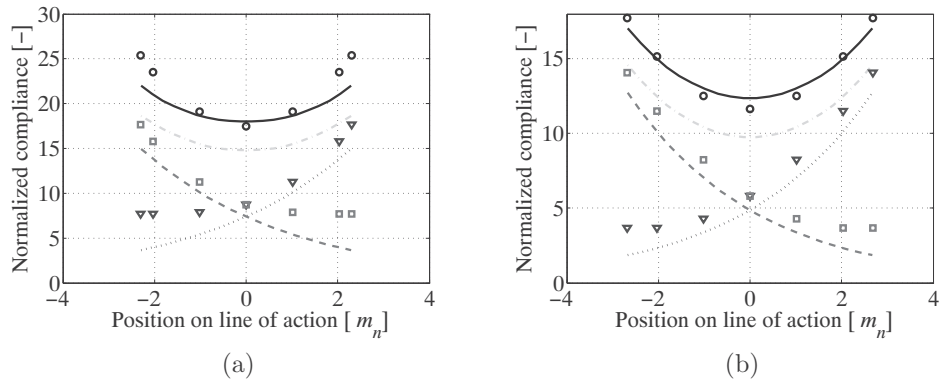
Figure 2.23: Single tooth and tooth pair compliance for (a) $z_1 = z_2 = 20$, and (b) $z_1 = z_2 = 70$. The markers represent Arafa and Megahed's values, and the lines show the results from the present model:
—∘ NC; ⋯▽ NC_1; --□ NC_2; -- $NC_1 + NC_2$

Figure 2.23(b) shows single tooth compliance and tooth pair compliance for the 70/70 gear pair. The results from the two models are practically identical for all contact positions.

Tooth pair stiffness Ziegler [3] presents measurements of tooth pair stiffnesses. In each of the measurements used here, the gear pair consists of two identical gears from which several teeth have been removed in order to measure the single tooth pair stiffness. The five gear pairs used are presented in table 2.4. The measured results have been read from the graphs presented

	Pair 1	Pair 2	Pair 3	Pair 4	Pair 5	Unit
z	49	48	46	44	38	-
x	0	0	0	0	0	-
b	17.75	17.75	17.75	17.75	17.75	mm
m_n	2.5	2.5	2.5	2.5	2.5	mm
α_n	20	20	20	20	20	deg
β	11°28'42"	16°15'37"	23°4'26"	28°21'27"	40°32'9"	deg

Table 2.4: Data for Ziegler's gear pairs

in [3, page 57], which gives an uncertainty. However this uncertainty is estimated to be a small percentage value, which is acceptable for the purpose of model validation. The measurements and the corresponding stiffnesses calculated with the present model are shown in figure 2.24. An excellent match between measurements and calculations are seen for all gear pairs.
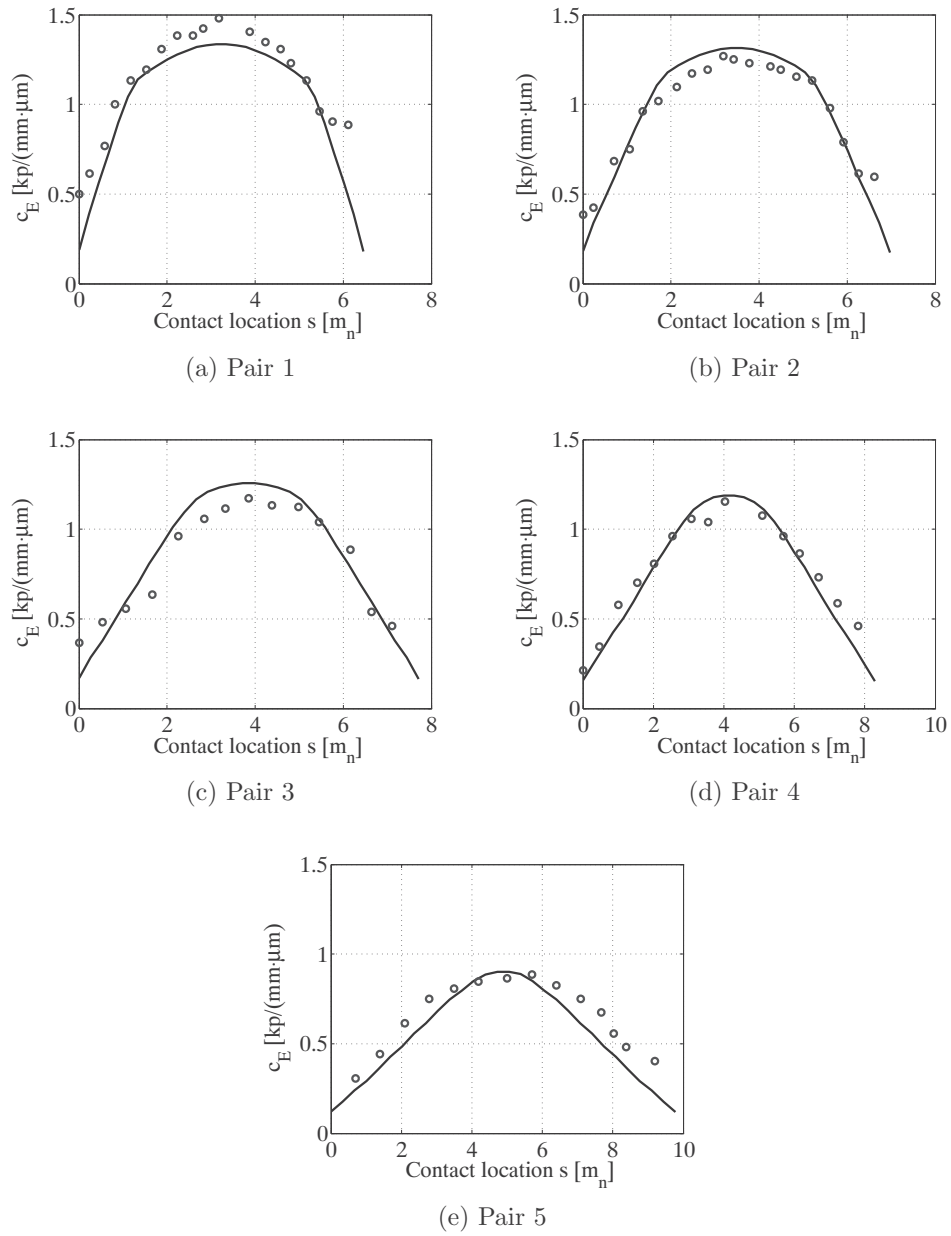
(a) Pair 1   (b) Pair 2

(c) Pair 3   (d) Pair 4

(e) Pair 5

Figure 2.24: Tooth pair stiffness compared to Ziegler [3]. The markers show the results from Ziegler's measurements

Gear mesh stiffness   The final set of gears used in the stiffness validation is loosely based on the intermediate stage of a 1 MW wind turbine gear box, except for a zero degree helix angle and zero profile shift on both gear and pinion is used. The basic data of the gear is presented in table 2.5. This stiffness of this gear set will be used in the time-varying modal analysis, which follows in section 3. The stiffness function found is validated by comparing to

	Driving gear	Driven gear	Unit
z	95	22	-
α_n	20		deg
β	0		deg
a	486		mm
m_n	8		mm
x	0	0	-
b	215	225	mm
M_t	74875.84	17339.67	Nm

Table 2.5: Basic gear data

results obtained using the commercial software KissSoft. The comparison is shown in figure 2.25. In figure 2.25(a) the gear mesh stiffness is shown, when deformations of the gear teeth are *not* included in the kinematic analysis to determine tooth contact positions. In this type of calculation, the total contact ratio for this spur gear pair equals the theoretical ϵ_α of 1.67. A good correlation between the models is seen. In figure 2.25(b), the elastic deformation in the gear mesh is included. In this case, the deformations cause the tooth to touch before the theoretical start of contact, and to stay in contact a longer period of time. This leads to an increase in contact ratio beyond the theoretical value. Also in this case a good correlation with the KissSoft results is shown.

2.6   Conclusion

A method for calculating gear mesh stiffness has been presented. For a number of gear geometries, the calculated results have been validated by comparison with theoretical and experimental results found in the literature.

The stiffness found will form the basis of the next chapters. First, the gear
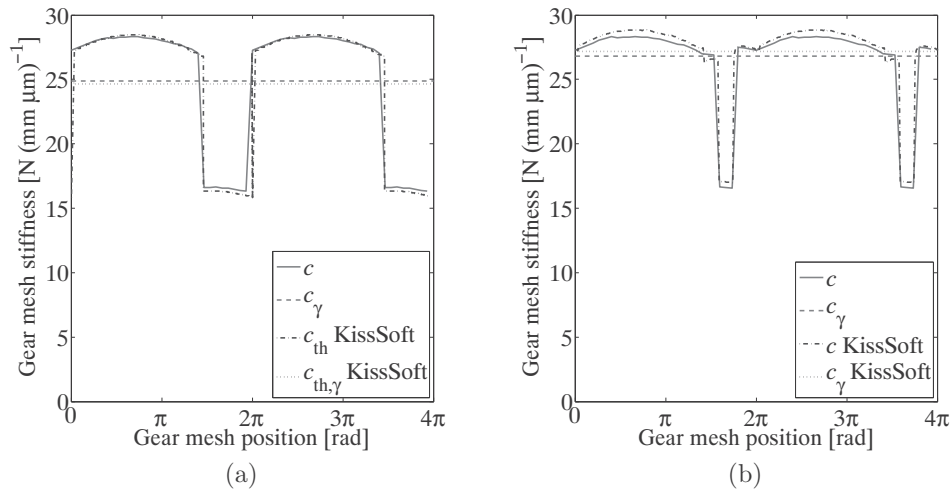
Figure 2.25: Validation of stiffness c and mean stiffness c_γ by comparing to program KissSoft: (a) No load-induced increase in contact ratio, (b) Including load-induced increase in contact ratio

mesh stiffness will be coupled with a very simple multibody model. This sample system is thoroughly investigated using the theory of time-varying modal analysis.

Chapter 3

Dynamic Coupling and Time-Varying Modal Analysis

The goal of this section is to apply the theory of time-varying modal analysis to the field of gear dynamics, which is one of the major contributions of this thesis. As an example gear set, a pair of spur gears is used instead of a complete gearbox. The gear mesh stiffness found in chapter 2 is the key component in the analysis. This simple example has been chosen in order to investigate the advantages and drawbacks of using the technique for analyzing vibrations in spur gears.

3.1 Introduction

Modal analysis method is very frequently used with the aim of integrating time-invariant linear equations of motion. The eigenvalues and eigenvectors obtained from the solution of eigenvalue problems allow engineers to interpret and visualize the dynamic behavior of different mechanical systems. For time-varying equations of motion the use of modal analysis in its well-know form is not possible. In this case a stability analysis normally relies on Floquet theory. The Floquet theory does not deliver the complete homogenous solution, but gives only information about the stability of the system represented by equations of motion with periodically varying coefficients (Ertz, Reister, Nordmann [62]).

In many cases as flexible rotating blades, flexible rotating discs, rotating

shafts with non-symmetrical cross section, and gear dynamics, the coefficients of the equations of motion vary periodically. In Xu and Gasch [63] the complete homogenous solution of *periodic* time-varying linear equations of motions is presented, based on Hill's approximation. The periodic time-varying matrix systems are expanded in Fourier series. Assuming that the solution also can be expanded in Fourier series, it is possible to obtain a general homogenous solution by solving a hyper-eigenvalue problem, i.e. when the number of Fourier coefficients is not infinite. The solution of the hyper-eigenvalue problem leads also to eigenvalues and eigenvectors; nevertheless, the eigenvectors become also periodic time-varying and the eigenvalues become dependent on the periodicity of the parameter variation. Different contributions to the problem of periodic time-varying modal analysis are presented in the literature, i.e. non-symmetric rotors (Ertz, Reister, Nordmann [62], Boru, Irretier [64]), flexible rotating discs (Irretier, Reuter [65], Reuter [66]), rotor-blade dynamics ([63], Santos, Saracho [67]) and later active control of rotor-blade dynamics (Christensen, Santos [68, 69, 70, 71]). The mathematical foundations of modal analysis for time-varying linear systems is clearly presented by Irretier in [72], and Bucher, Ewins in [73].

In [62] the dynamics of a simple flexible shaft with non-symmetric cross section, supported by anisotropic bearings, is theoretically investigated using Hill's approach. In [64] such an investigation is carried out theoretically as well experimentally.

Flexible rotating discs are also examples of periodically time-varying structures. Their dynamics are carefully investigated using periodic time varying modal analysis in [65, 66]. The theoretical work in presented in [65], and the experimental validation in [66], illustrates the continuation of Irretier's work [74].

Rotating flexible blades are also examples of periodically time-varying systems. Their dynamics are also carefully investigated using periodic time-varying modal analysis, as can be seen in [63], Bienert [75], and in [67, 76]. In [76] a contribution to the experimental validation of linear and nonlinear dynamic models for representing rotor-blades parametrically coupled vibrations is given. The rotor-blade dynamics is described by using three models with different levels of complexity followed by experimental validation of such models. A deeper physical understanding of the dynamic coupling and the

behavior of the parametric vibrations is achieved. Such an understanding is of fundamental importance while developing active control strategies. In [68] the design of time-varying modal controllers is in focus. Time-varying modal analysis and modern control theory are integrated in an elegant way allowing the development of new control strategies. The modal controllability and observability of bladed discs are strongly dependent on the angular velocity; a detailed analysis of such a dependency is presented in [69]. To control rotor and blade vibration using only shaft actuation is a challenging problem. In [70] such a problem is investigated theoretically as well as experimentally using different control strategies. Electromagnetic actuators are used to control a horizontal rotor-blade system (blades periodically excited by the gravity). In [71] the same problem is theoretically as well as experimentally investigated and new strategies are developed to control vertical rotor-blade systems.

3.2 Mathematical Modeling

The gear mesh stiffness is calculated for several relative positions of the meshing gears as described in section 2. This gives a load- and position-dependent stiffness. Under the high loads considered in the following dynamic analysis, it is assumed that tooth separation will not occur. After completing the stiffness calculation, a constant angular velocity is assumed. By these assumptions, the gear mesh stiffness becomes a periodically varying parameter in the time domain, that is, the nonlinearity is removed. It must also be noted that all teeth are considered identical, i.e. pitch errors are not included. The resulting system can be investigated using the theory for modal analysis of linear time-varying systems.

When the only time-varying parameter in the system is the gear mesh stiffness, the equation of motion can be written as

$$\mathbf{M}\ddot{\mathbf{q}} + \mathbf{C}\dot{\mathbf{q}} + \mathbf{K}(t)\mathbf{q} = \mathbf{f} \tag{3.1}$$

$$\Updownarrow$$

$$\begin{bmatrix} \dot{\mathbf{q}} \\ \ddot{\mathbf{q}} \end{bmatrix} - \begin{bmatrix} \mathbf{0} & \mathbf{I} \\ \mathbf{M}^{-1}\mathbf{K}(t) & \mathbf{M}^{-1}\mathbf{C} \end{bmatrix} \begin{bmatrix} \mathbf{q} \\ \dot{\mathbf{q}} \end{bmatrix} = \begin{bmatrix} \mathbf{0} & \mathbf{0} \\ \mathbf{0} & \mathbf{M}^{-1} \end{bmatrix} \begin{bmatrix} \mathbf{0} \\ \mathbf{f} \end{bmatrix} \tag{3.2}$$

or

$$\dot{\mathbf{z}} - \mathbf{A}(t)\mathbf{z} = \mathbf{p}, \ \mathbf{z} = \begin{bmatrix} \mathbf{q} \\ \dot{\mathbf{q}} \end{bmatrix}, \ \mathbf{A}(t) = \mathbf{A}(t+T) \tag{3.3}$$

The first part of the analysis of equation (3.3) involves the homogeneous part of the equation, that is, $\dot{\mathbf{z}} - \mathbf{A}(t)\mathbf{z} = \mathbf{0}$. This equation is analyzed by expanding the theory of modal analysis of time-invariant systems [59] to include periodically time-varying parameters, as shown in [67] and [63]. By the substitutions

$$\mathbf{z}(t) = \mathbf{r}(t)e^{\lambda t} \Rightarrow \dot{\mathbf{z}}(t) = \dot{\mathbf{r}}(t)e^{\lambda t} + \lambda\mathbf{r}(t)e^{\lambda t} \tag{3.4}$$

$$\mathbf{p} = \mathbf{0} \tag{3.5}$$

into equation (3.3), the equation can be written as the eigenvalue problem

$$\dot{\mathbf{r}}(t) + \lambda\mathbf{r}(t) - \mathbf{A}(t)\mathbf{r}(t) = \mathbf{0} \tag{3.6}$$

$$\Updownarrow$$

$$\dot{\mathbf{r}}(t) + \big(\lambda\mathbf{I} - \mathbf{A}(t)\big)\mathbf{r}(t) = \mathbf{0} \tag{3.7}$$

Under the assumption of constant angular velocity, the gear mesh frequency in units rad/sec is called Ω. The stiffness matrix $\mathbf{K}(t)$ and therefore the state matrix $\mathbf{A}(t)$ are both periodic with period $T = 2\pi/\Omega$ and can be expanded as infinite, complex Fourier series. Also the time-varying eigenvector $\mathbf{r}_j(t)$, belonging to the jth eigenvalue, is assumed to be periodic. In all equations, i$= \sqrt{-1}$.

$$\mathbf{K}(t) = \sum_{k=-\infty}^{\infty} \mathbf{K}_k e^{ik\Omega t} \tag{3.8}$$

$$\mathbf{A}(t) = \sum_{a=-\infty}^{\infty} \mathbf{A}_a e^{ia\Omega t} \tag{3.9}$$

$$\mathbf{r}_j(t) = \sum_{r=-\infty}^{\infty} \mathbf{r}_{j,r} e^{ir\Omega t} \text{ for } j = 1\dots2N \tag{3.10}$$

It can be shown [63] that the components of the eigenvectors $\mathbf{r}_j(t)$ can be found by re-writing equation (3.7):

$$\left(\lambda_j\hat{\mathbf{I}} - \hat{\mathbf{A}}\right)\begin{bmatrix} \dots \\ \mathbf{r}_{j,-2} \\ \mathbf{r}_{j,-1} \\ \mathbf{r}_{j,0} \\ \mathbf{r}_{j,1} \\ \mathbf{r}_{j,2} \\ \dots \end{bmatrix} = \begin{bmatrix} \dots \\ \mathbf{0} \\ \mathbf{0} \\ \mathbf{0} \\ \mathbf{0} \\ \mathbf{0} \\ \dots \end{bmatrix} \tag{3.11}$$

where

$$
\hat{\mathbf{A}} =
\begin{bmatrix}
\ddots & \cdots & \cdots & \cdots & \cdots & \cdots & \cdots \\
\cdots & 2\mathrm{i}\Omega\mathbf{I} + \mathbf{A}_0 & \mathbf{A}_{-1} & \mathbf{A}_{-2} & \mathbf{A}_{-3} & \mathbf{A}_{-4} & \cdots \\
\cdots & \mathbf{A}_1 & \mathrm{i}\Omega\mathbf{I} + \mathbf{A}_0 & \mathbf{A}_{-1} & \mathbf{A}_{-2} & \mathbf{A}_{-3} & \cdots \\
\cdots & \mathbf{A}_2 & \mathbf{A}_1 & \mathbf{A}_0 & \mathbf{A}_{-1} & \mathbf{A}_{-2} & \cdots \\
\cdots & \mathbf{A}_3 & \mathbf{A}_2 & \mathbf{A}_1 & -\mathrm{i}\Omega\mathbf{I} + \mathbf{A}_0 & \mathbf{A}_{-1} & \cdots \\
\cdots & \mathbf{A}_4 & \mathbf{A}_3 & \mathbf{A}_2 & \mathbf{A}_1 & -2\mathrm{i}\Omega\mathbf{I} + \mathbf{A}_0 & \cdots \\
\cdots & \cdots & \cdots & \cdots & \cdots & \cdots & \ddots
\end{bmatrix}
$$

$$(3.12)$$

In an exact solution to equation (3.11), $\hat{\mathbf{A}}$ is of infinite dimension. However, the magnitude of the Fourier components of $\mathbf{A}(t)$ depends directly on the Fourier components of $\mathbf{K}(t)$. Therefore, if the gear mesh stiffness function included in $\mathbf{K}(t)$ is smooth, only a few of the Fourier components of $\mathbf{A}(t)$ will have a magnitude that will significantly influence the resulting displacements and velocities in vector $\mathbf{z}(t)$. In a later section, it will be shown how to calculate the necessary number of Fourier components to be included in $\hat{\mathbf{A}}$, in order to obtain accurate results. If the number of included Fourier components is n, in the sense that

$$
\mathbf{K}(t) = \sum_{k=-n}^{n} \mathbf{K}_k \mathrm{e}^{\mathrm{i}k\Omega t} \tag{3.13}
$$

and the number of degrees of freedom in the model is N, the dimension of matrix $\hat{\mathbf{A}}$ will be $2N(2n+1) \times 2N(2n+1)$.

There is a great amount of redundant information in the solution of equation (3.11). Only the basis eigenvalues and basis eigenvectors, which are identified as described in a later section, are needed in the ensuing analysis. The $2N$ basis eigenvalues are stored in a diagonal matrix $\mathbf{\Lambda}$, and the Fourier components of the basis eigenvectors $\mathbf{r}_{j,0}$ are stored in the 3-dimensional array $\mathbf{R}$. This array can be visualized as $(2n+1)$ "layers" of $2N \times 2N$ matrices. The kth layer of $\mathbf{R}$ will have the structure $\mathbf{R}_k = [\mathbf{r}_{1,k} \ \mathbf{r}_{2,k} \ \cdots \ \mathbf{r}_{2N-1,k} \ \mathbf{r}_{2N,k}]$ for $k = -n \ldots n$

To find the solution $\mathbf{q}$ of equation (3.1), also the left eigenvectors $\mathbf{L}(t)$, which are the solution to the equation $\mathbf{R}(t)\mathbf{L}(t) = \mathbf{I}$ are needed. These can be

found by solving the matrix equation:

$$\mathbf{R}(t)\mathbf{L}(t) = \mathbf{I} \tag{3.14}$$

$\Updownarrow$

$$\sum_{r=-\infty}^{\infty} \mathbf{R}_r \mathrm{e}^{ir\Omega t} \sum_{l=-\infty}^{\infty} \mathbf{L}_l \mathrm{e}^{il\Omega t} = \mathbf{I} \tag{3.15}$$

$\Updownarrow$

$$\begin{bmatrix} \cdots & \cdots & \cdots & \cdots & \cdots & \cdots & \cdots \\ \cdots & \mathbf{R}_0 & \mathbf{R}_{-1} & \mathbf{R}_{-2} & \mathbf{R}_{-3} & \mathbf{R}_{-4} & \cdots \\ \cdots & \mathbf{R}_1 & \mathbf{R}_0 & \mathbf{R}_{-1} & \mathbf{R}_{-2} & \mathbf{R}_{-3} & \cdots \\ \cdots & \mathbf{R}_2 & \mathbf{R}_1 & \mathbf{R}_0 & \mathbf{R}_{-1} & \mathbf{R}_{-2} & \cdots \\ \cdots & \mathbf{R}_3 & \mathbf{R}_2 & \mathbf{R}_1 & \mathbf{R}_0 & \mathbf{R}_{-1} & \cdots \\ \cdots & \mathbf{R}_4 & \mathbf{R}_3 & \mathbf{R}_2 & \mathbf{R}_1 & \mathbf{R}_0 & \cdots \\ \cdots & \cdots & \cdots & \cdots & \cdots & \cdots & \cdots \end{bmatrix} \begin{bmatrix} \cdots \\ \mathbf{L}_{-2} \\ \mathbf{L}_{-1} \\ \mathbf{L}_0 \\ \mathbf{L}_1 \\ \mathbf{L}_2 \\ \cdots \end{bmatrix} = \begin{bmatrix} \cdots \\ \mathbf{0} \\ \mathbf{0} \\ \mathbf{I} \\ \mathbf{0} \\ \mathbf{0} \\ \cdots \end{bmatrix} \tag{3.16}$$

In most practical cases, the magnitudes of the submatrices $\mathbf{R}_n$ will decrease with increasing n. Therefore, a solution based on the central rows and columns of the infinitely large system of Eqs. (3.16) will be sufficiently accurate. For $n = 2$, equation (3.16) can be approximated by:

$$\begin{bmatrix} \mathbf{R}_0 & \mathbf{R}_{-1} & \mathbf{R}_{-2} & \mathbf{0} & \mathbf{0} \\ \mathbf{R}_1 & \mathbf{R}_0 & \mathbf{R}_{-1} & \mathbf{R}_{-2} & \mathbf{0} \\ \mathbf{R}_2 & \mathbf{R}_1 & \mathbf{R}_0 & \mathbf{R}_{-1} & \mathbf{R}_{-2} \\ \mathbf{0} & \mathbf{R}_2 & \mathbf{R}_1 & \mathbf{R}_0 & \mathbf{R}_{-1} \\ \mathbf{0} & \mathbf{0} & \mathbf{R}_2 & \mathbf{R}_1 & \mathbf{R}_0 \end{bmatrix} \begin{bmatrix} \mathbf{L}_{-2} \\ \mathbf{L}_{-1} \\ \mathbf{L}_0 \\ \mathbf{L}_1 \\ \mathbf{L}_2 \end{bmatrix} = \begin{bmatrix} \mathbf{0} \\ \mathbf{0} \\ \mathbf{I} \\ \mathbf{0} \\ \mathbf{0} \end{bmatrix} \tag{3.17}$$

With $\mathbf{L}_l$ found for $l = -n \cdots n$, the solutions to the homogeneous and the inhomogeneous equation of motion, equation (3.1), can now be found [67, 63]. First, equation (3.6) is rewritten as

$$\mathbf{r}(t)\lambda + \dot{\mathbf{r}}(t) - \mathbf{A}(t)\mathbf{r}(t) = \mathbf{0} \tag{3.18}$$

which is then expanded from a vector equation to a matrix equation to include all eigenvalues and eigenvectors simultaneously:

$$\mathbf{R}(t) \begin{bmatrix} \ddots & & \\ & \lambda_k & \\ & & \ddots \end{bmatrix} + \dot{\mathbf{R}}(t) - \mathbf{A}(t)\mathbf{R}(t) = \mathbf{0} \tag{3.19}$$

The equation above is multiplied from the left with $\mathbf{L}(t)$ while using the property $\mathbf{L}(t)\mathbf{R}(t) = \mathbf{I}$, and rearranged:

$$\mathbf{L}(t)\mathbf{R}(t)\begin{bmatrix} \ddots & & \\ & \lambda_k & \\ & & \ddots \end{bmatrix} + \mathbf{L}(t)\dot{\mathbf{R}}(t) - \mathbf{L}(t)\mathbf{A}(t)\mathbf{R}(t) = \mathbf{0} \quad (3.20)$$

$\Updownarrow$

$$\begin{bmatrix} \ddots & & \\ & \lambda_k & \\ & & \ddots \end{bmatrix} = -\mathbf{L}(t)\dot{\mathbf{R}}(t) + \mathbf{L}(t)\mathbf{A}(t)\mathbf{R}(t) \quad (3.21)$$

This result is needed later in the analysis. Now the modal coordinates $\mathbf{y}(t)$ are introduced as

$$\mathbf{z}(t) = \mathbf{R}(t)\mathbf{y}(t) \Rightarrow \dot{\mathbf{z}}(t) = \dot{\mathbf{R}}(t)\mathbf{y}(t) + \mathbf{R}(t)\dot{\mathbf{y}}(t) \quad (3.22)$$

This is inserted into equation (3.3), and all terms are multiplied from the left with $\mathbf{L}(t)$, which yields

$$\mathbf{L}(t)\dot{\mathbf{R}}(t)\mathbf{y}(t) + \mathbf{L}(t)\mathbf{R}(t)\dot{\mathbf{y}}(t) - \mathbf{L}(t)\mathbf{A}(t)\mathbf{R}(t)\mathbf{y}(t) = \mathbf{L}(t)\mathbf{p} \quad (3.23)$$

$\Updownarrow$

$$\dot{\mathbf{y}}(t) + \Big(\mathbf{L}(t)\dot{\mathbf{R}}(t) - \mathbf{L}(t)\mathbf{A}(t)\mathbf{R}(t)\Big)\mathbf{y}(t) = \mathbf{L}(t)\mathbf{p} \quad (3.24)$$

Now equation (3.21) is inserted, and the result is the decoupled modal equations of motion

$$\dot{\mathbf{y}}(t) - \begin{bmatrix} \ddots & & \\ & \lambda_k & \\ & & \ddots \end{bmatrix}\mathbf{y}(t) = \mathbf{L}(t)\begin{bmatrix} \mathbf{0} \\ \mathbf{M}^{-1} \end{bmatrix}\mathbf{f}(t) \quad (3.25)$$

By inserting $\mathbf{L}(t) = \sum_{l=-n}^{n} \mathbf{L}_l e^{il\Omega t}$ and the oscillating force $\mathbf{f}(t) = \mathbf{p}^{+}e^{i\Omega^{*}t}$ into the right hand side of (3.25), the equation becomes

$$\dot{\mathbf{y}}(t) - \begin{bmatrix} \ddots & & \\ & \lambda_k & \\ & & \ddots \end{bmatrix}\mathbf{y}(t) = \sum_{l=-n}^{n} \mathbf{L}_l\begin{bmatrix} \mathbf{0} \\ \mathbf{M}^{-1} \end{bmatrix}\mathbf{p}^{+}e^{i(\Omega^{*}+l\Omega)t} \quad (3.26)$$

Now a modal solution $\mathbf{y}(t)$ with the same frequency as the forcing function in equation (3.26) is assumed:

$$\mathbf{y}(t) = \mathbf{y}e^{i(\Omega^* + l\Omega)t} \Rightarrow \dot{\mathbf{y}}(t) = \mathbf{y}i(\Omega^* + l\Omega)e^{i(\Omega^* + l\Omega)t} \qquad (3.27)$$

This solution is inserted into (3.26), which yields

$$i(\Omega^* + l\Omega)\mathbf{y}(t) - \begin{bmatrix} \ddots & & \\ & \lambda_k & \\ & & \ddots \end{bmatrix} \mathbf{y}(t) = \sum_{l=-n}^{n} \mathbf{L}_l \begin{bmatrix} \mathbf{0} \\ \mathbf{M}^{-1} \end{bmatrix} \mathbf{p}^+ e^{i(\Omega^* + l\Omega)t} \quad (3.28)$$

$$\Leftrightarrow \begin{bmatrix} \ddots & & \\ & i(\Omega^* + l\Omega) - \lambda_k & \\ & & \ddots \end{bmatrix} \mathbf{y}(t) = \sum_{l=-n}^{n} \mathbf{L}_l \begin{bmatrix} \mathbf{0} \\ \mathbf{M}^{-1} \end{bmatrix} \mathbf{p}^+ e^{i(\Omega^* + l\Omega)t}$$

$$(3.29)$$

The transformation back to the $\mathbf{z}(t)$ coordinates is performed using equation (3.22), and $\mathbf{R}(t)$ is substituted by its equivalent sum $\sum_{r=-n}^{n} \mathbf{R}_r$. The resulting equation shows the forced response:

$$\mathbf{z}_{\text{inhom}}(t) = \sum_{r=-n}^{n} \sum_{l=-n}^{n} \mathbf{R}_r \begin{bmatrix} \ddots & & \\ & \frac{1}{i(\Omega^* + l\Omega) - \lambda_k} & \\ & & \ddots \end{bmatrix} \mathbf{L}_l \begin{bmatrix} \mathbf{0} \\ \mathbf{M}^{-1} \end{bmatrix} \mathbf{p}^+ e^{i(\Omega^* + \Omega(r+l))t}$$

$$(3.30)$$

When using a finite n and the initial condition $\mathbf{z}(t_0) = \mathbf{z}_0$, the solution to the homogeneous equation of motion is very similar in form to the homogeneous solution for a time-invariant system:

$$\mathbf{z}_{\text{hom}}(t) = \mathbf{R}(t) \begin{bmatrix} \ddots & & \\ & e^{\lambda_k(t-t_0)} & \\ & & \ddots \end{bmatrix} \mathbf{L}(t_0)\mathbf{z}_0 \qquad (3.31)$$

To find the basis eigenvectors and basis eigenvalues needed to set up $\mathbf{R}(t)$ and λ_k in equation (3.30), the eigenvalues and corresponding vectors must be sorted. This sorting is also necessary to correctly calculate the eigenvector normalization factors, as described in a later section. The problem can be described by figure 3.1, in which the imaginary part of the eigenvalues is plotted versus the gear mesh angular velocity Ω. Both figures are zoomed
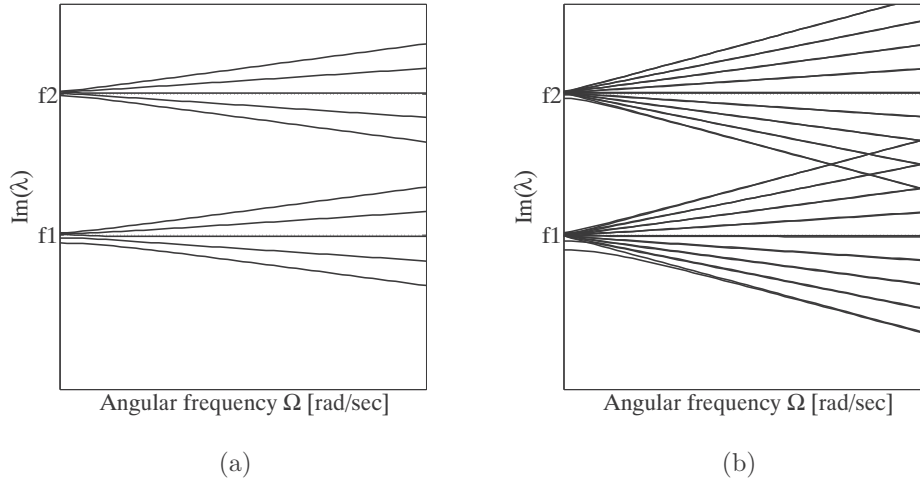
Figure 3.1: Solutions to hyper-eigenvalue problem: (a) Low n or low Ω, (b) High n or high Ω

in to show only two "families" of eigenfrequencies. In figure 3.1(a), $n = 2$ Fourier components are included in the analysis. Here, the sorting is easy: the $2n+1$ lower frequencies belong to the low-frequency family centered around f_1. In figure 3.1(b), $n = 4$ and the situation is more complicated; it is no longer a trivial task to decide which eigenvalues belong to which family. A typical eigenvalue distribution in the complex plane is shown in figure 3.2(a). It is clear how the different families of eigenvalues can be identified by their real part, which is nearly identical for all members of the family [63]. This method will solve the problem visualized in figure 3.1(b). However, because of the transformation into state space from equation (3.1) to equation (3.3), the eigenvalues are found in complex conjugate pairs, as depicted in figures 3.2(a) and 3.2(b). Obviously, these cannot be separated based on their real part alone. Instead, a sorting algorithm based on a first order Taylor expansion of the eigenvalues as a function of Ω is used. For a given Ω_k, where k is an integer index, the expected value for λ is given by

$$\lambda_{k,\text{expected}} = \lambda_{k-1} + \frac{\mathrm{d}\lambda}{\mathrm{d}\Omega}\Delta\Omega \approx \lambda_{k-1} + \frac{\lambda_{k-1} - \lambda_{k-2}}{\Omega_{k-1} - \Omega_{k-2}}\left(\Omega_k - \Omega_{k-1}\right) \qquad (3.32)$$
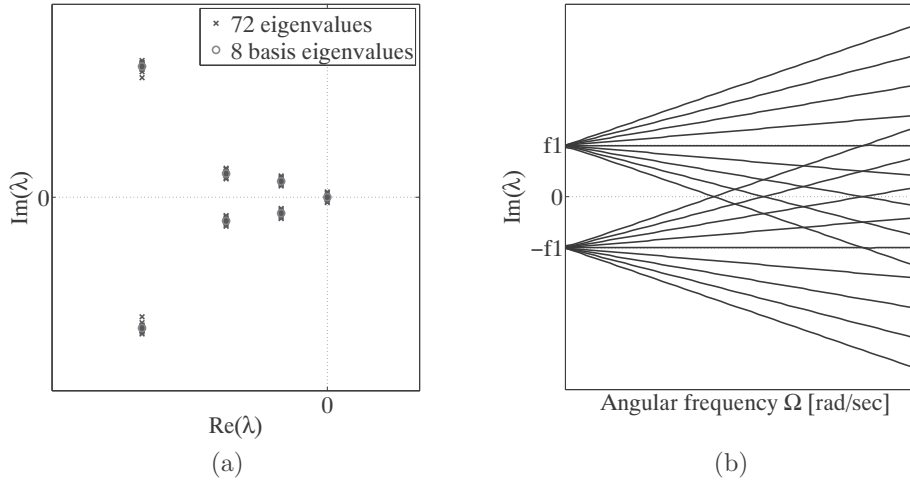
Figure 3.2: Complex conjugate eigenvalues: (a) Eigenvalue distribution, (b) High n or high Ω

The eigenvalues $\lambda_{k,\text{expected}}$ predicted by equation (3.32) are then compared to those actually obtained by solving the hyper-eigenvalue problem, λ_k. The absolute difference between $\lambda_{k,\text{expected}}$ and λ_k is calculated, and the eigenvalues in λ_k are then identified with the eigenvalue in $\lambda_{k,\text{expected}}$, which shows the minimum difference. A few requirements must be fulfilled in order to use the Taylor expansion sorting method:

1. The hyper-eigenvalue problem must be solved for a monotonically increasing value of Ω

2. At least two solutions, for $k-2$ and for $k-1$ must be computed without the Taylor expansion sorting

3. The values of Ω should not increase too much in each step in order to get a good estimation of λ_k from equation (3.32), i.e., a certain smoothness of the function $\lambda(\Omega)$ is required.

When the eigenvalues have been sorted within each family, the families are sorted relative to each other based on the mean value of the imaginary part of the eigenvalues in the family. The basis eigenvalues are now defined as the central member of the family, based on the imaginary part.

3.3 Results

The gear pair, the attached shafts and the inertias $J_1 \ldots J_4$ are shown in figure 3.3. The degrees of freedom (DOF) of the model are the angles of rotation of the four inertias and will be referred to as $\mathbf{q} = [q_1 \ q_2 \ q_3 \ q_4]^T$. The model has intentionally been kept very simple in order to keep the results easy to interpret. Since no lateral DOFs are included, gyroscopic effects are not considered in the utilized model. The gear mesh stiffness function,
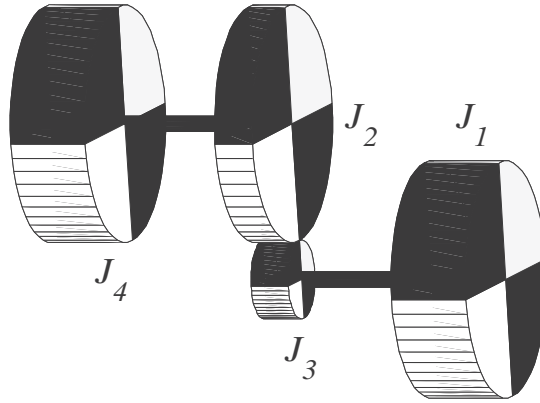

Figure 3.3: System model

which was calculated in section 2 and validated by comparison to KissSoft calculations in section 2.5 is shown in figure 3.4(a). For a constant angular velocity Ω, the periodic stiffness can be described using its complex Fourier expansion. When t is time, the Fourier series is defined as

$$c(t) = \sum_{j=-\infty}^{\infty} c_j \mathrm{e}^{\mathrm{i}jt} \tag{3.33}$$

In figure 3.4(b), the first 30 Fourier components of the signals are shown, expressed as $A_j = 2|c_j|$. Because of the symmetry in the complex Fourier components, where $c_j = \bar{c}_{-j}$, only c_j for $j = 1 \cdots 30$ are shown. The mean value of the gear mesh stiffness $c_0 = 26.66$ N (mm μm)$^{-1}$ is not shown in order to illustrate the other components more clearly. To identify each of the $2N$ eigenfrequencies and the associated eigenvectors, a time-invariant $(n = 0)$
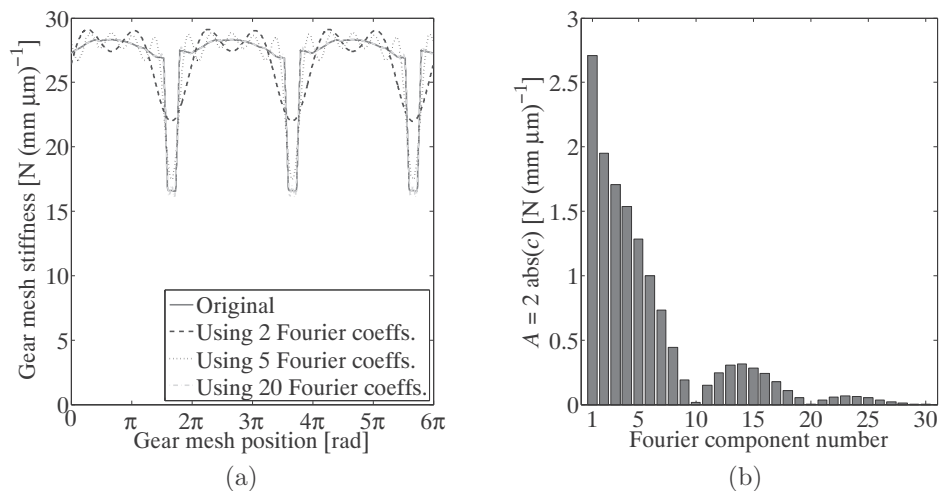
Figure 3.4: (a) Gear mesh stiffness, (b) Fourier expansion of gear mesh stiffness

calculation has been performed. The $2N$ modes are numbered according to table 3.1. The mode shapes $\mathbf{r}_j(t)$ can be evaluated at a given time t using the

Mode no.	Frequency
1	0 Hz
2	0 Hz
3	399 Hz
4	-399 Hz
5	585 Hz
6	-585 Hz
7	3216 Hz
8	-3216 Hz

Table 3.1: Fundamental eigenfrequencies for $n = 0$

formula (3.10), using $-n$ and n as the limits for the sum. The result is shown in figure 3.5 for $n = 10$, where the displacement parts of the eigenvectors are plotted versus the gear mesh position θ in the interval $[0,2\pi]$, corresponding to the time interval $[0,T]$ at a constant gear mesh angular velocity Ω. Modes 1 and 2 - the rigid body modes - directly show the gear ratio 95/22. Modes
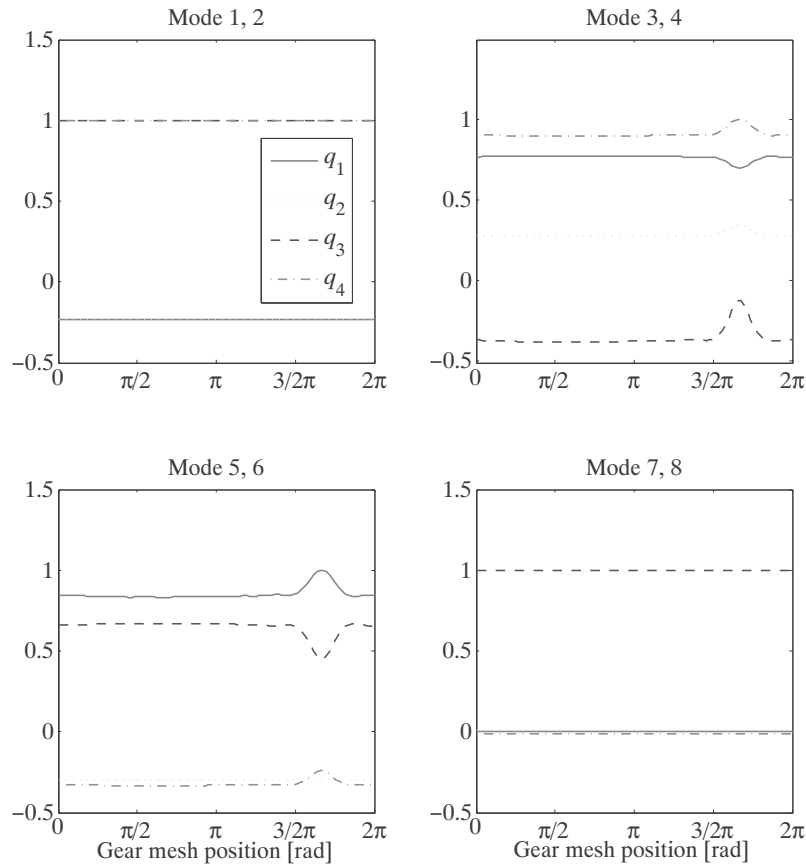
Figure 3.5: Mode shapes as a function of gear mesh position $\theta = \Omega t$, calculated for $n = 10$

3 through 8 are elastic modes showing torsional deformations in the shafts and the gear mesh. It can be seen how modes 3,4,5, and 6 are strongly affected by the varying stiffness, while modes 1,2,7, and 8 are almost constant, $\mathbf{r}_1(t) \approx \mathbf{r}_1, \mathbf{r}_2(t) \approx \mathbf{r}_2$, $\mathbf{r}_7(t) \approx \mathbf{r}_7$, and $\mathbf{r}_8(t) \approx \mathbf{r}_8$.

As a preliminary analysis, the eigenfrequencies for the system can be calculated "quasi-statically" for a given time $t = t_1$. To do this, $\mathbf{A}(t)$ in equation (3.7) is evaluated at $t = t_1$ using the first $2n+1$ terms in equation (3.9),

where n is the number of Fourier components included in the analysis:

$$\mathbf{A}(t_1) = \sum_{a=-n}^{n} \mathbf{A}_a \mathrm{e}^{\mathrm{i}a\Omega t_1} \tag{3.34}$$

$\mathbf{A}(t_1)$ is then inserted into equation (3.7), and the eigenvalue problem is solved. The resulting (positive) eigenfrequencies are shown in figure 3.6 for two different values of n. From the figure, it can be seen that the highest
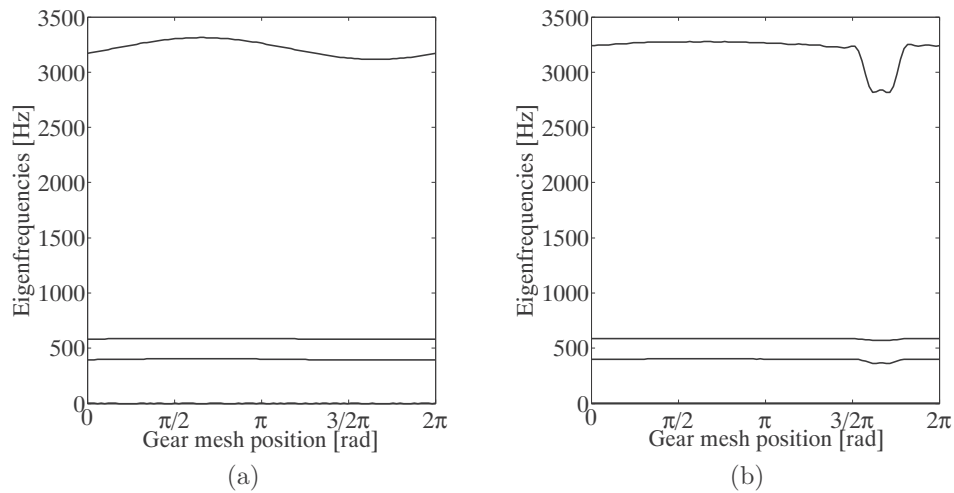

Figure 3.6: "Quasi-static" eigenfrequency analysis: (a) $n = 1$, (b) $n = 18$

eigenfrequency at roughly 3200 Hz is much more sensitive to the variations in the gear mesh stiffness than the other eigenfrequencies. Also, n has an influence on the extent of the frequency interval, in which the highest eigenfrequency is located. As a conclusion to this "quasi-static" analysis, n can be expected to play an important role when determining the free and the forced response of the time-varying system.

The accuracy of the time-varying modal analysis depends on the number of Fourier components, n, included in the analysis. When the applied force $\mathbf{f}$ in equation (3.1) is constant or zero, only the changing stiffness in $\mathbf{K}(t)$ can excite the system. From equation (3.13), it can be expected, that only frequencies up to approximately $f = n\Omega$ will be excited. From the time-

invariant modal analysis of the system it is known that the highest eigenfrequency is around 3215 Hz. When the gear mesh frequency is $\Omega = 1357.59$ rad/sec ≈ 216 Hz, this eigenfrequency can be expected to be excited only when $n \geq 3215/216 \approx 15$.

The accuracy of the method can be determined by comparing the solution in the time domain to the corresponding solution obtained by numerical integration. For this purpose, q_3 has been chosen, as this DOF shows the largest difference between the two calculation methods, as seen from figure 3.7(a). It might be interesting to represent the time variations of the dynamic mesh force (as opposed to q_3 in figure 3.7) since it also gives an indication on the presence of nonlinearity (contact losses when the mesh force is negative). Since this loss of contact is not considered in the present gear mesh model, the dynamic mesh force is calculated as the difference between the displacements of the two gears multiplied by the mesh stiffness, $F(t) = c(t)\Big(q_3(t)r_3 - q_2(t)r_2\Big)$, where r_2 and r_3 are the radii of the two gears. Comparison based on a single DOF is the simplest way, since $F(t)$ offers no new information on the dynamic behavior of the system. It is clear from figure 3.7(a) that the accuracy of the modal solution increases significantly when n reaches 15. An increase in n beyond 18 does not increase accuracy much. A zoom-in of the two solutions is shown in figure 3.7(b).

For each number of n, the eigenvalue problem, equation (3.11), changes. It can therefore be expected, that both the fundamental eigenfrequencies (for $k = 0$) and the higher-order parametric eigenfrequencies (for $k \in [-n, n]$, $k \neq 0$) will change as a function of n. In the following analysis, the change in the fundamental eigenfrequencies, evaluated at the nominal speed $\Omega = 1357.59$ rad/sec, is investigated. The results are shown in figure 3.8, where the per cent change of the eigenfrequencies belonging to the 3 elastic modes, relative to a time-invariant modal analysis ($n = 0$) are plotted. It can be seen that there are no significant changes in the fundamental eigenfrequencies. At no point do the frequencies change more than 0.16 per cent.

For each of the $2N$ eigenvectors, the importance of the kth harmonic parametric vibration mode can be calculated. This is done by finding the relative magnitude of the harmonic components of the eigenvector. For the kth harmonic component of the jth eigenvector, $\mathbf{r}_{j,k}$, the Normalization Factor $\text{NF}_{j,k}$
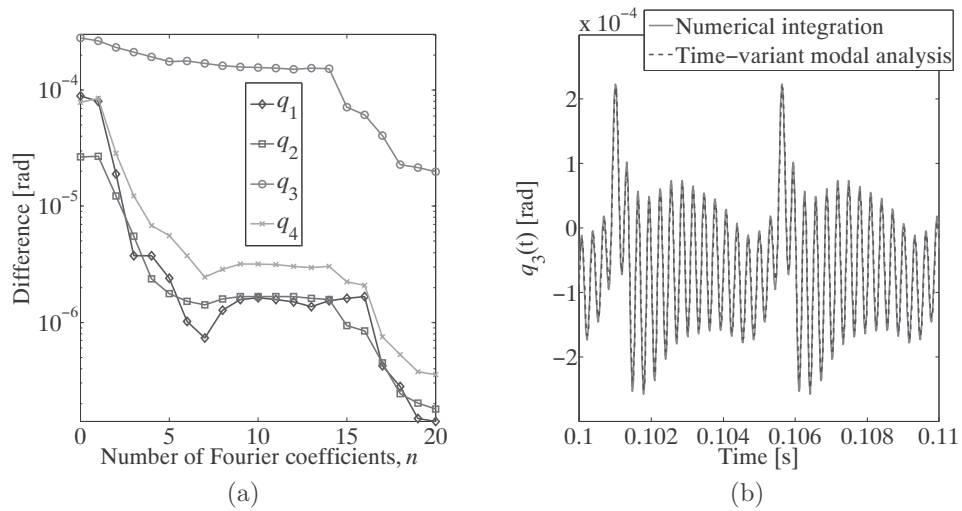
Figure 3.7: Comparison of solutions: (a) Maximum difference between numerical integration and time-varying modal analysis, (b) Comparison of time-domain solutions (zoom). Only $q_3(t)$ is shown
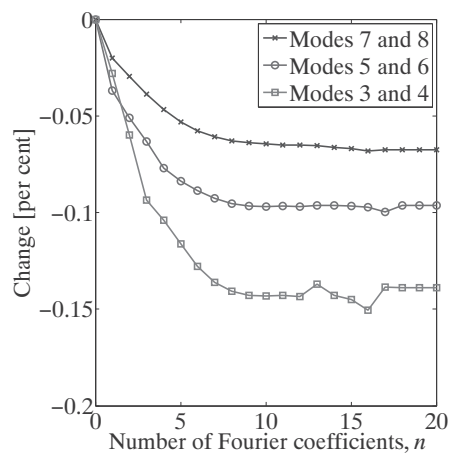

Figure 3.8: Change in fundamental frequencies

is defined as:

$$
\mathrm{NF}_{j,k} = \frac{1}{\sqrt{\mathbf{r}_{j,k}^T \mathbf{r}_{j,k}}} \quad \text{with } \mathbf{r}_j = \begin{bmatrix} \mathbf{r}_{j,-n} \\ \dots \\ \mathbf{r}_{j,-1} \\ \mathbf{r}_{j,0} \\ \mathbf{r}_{j,1} \\ \dots \\ \mathbf{r}_{j,n} \end{bmatrix} \quad \text{for } j = 1 \dots 2N \qquad (3.35)
$$

In figures 3.9 and 3.10, normalization factors for all 8 modes are plotted versus the gear mesh frequency Ω (in rad/sec), for $n = 3$ and $n = 10$, respectively. The NF-axes in the plots are logarithmic and show the interval $\mathrm{NF} \in [10^{-2}, 10^1]$. NF for the fundamental harmonic component, $k = 0$, is set to $\mathrm{NF}_{j,0} = 1$ in all cases. With these definitions, the normalization factors show how the fundamental part of the mode shape vector $\mathbf{r}_0$ is related to the time-varying parts $\mathbf{r}_k$ for $k = -n \dots n$ depending on the operational speed Ω. The kth harmonic component showing the smallest $\mathrm{NF}_{j,k}$ will be predominant in the jth mode shape at a particular gear mesh frequency Ω. A number of observations can be made from the normalization factor plots, figures 3.9 and 3.10:

1. For the rigid-body modes 1 and 2, the fundamental harmonic $k = 0$ is predominant for all gear mesh frequencies $\Omega > 0$.

2. For all elastic modes, there is a symmetry between the positive (left column) and the negative frequencies (right column in the plots): For the jth positive eigenfrequency, the normalization factor $\mathrm{NF}_{j,k}$ is equal to $\mathrm{NF}_{j,-k}$ for the corresponding negative eigenfrequency.

3. For modes 3, 4, 5, and 6, there exist certain mesh frequency ranges, for which the time-varying part of the mode shape (parametric vibrations) will be more important than the stationary part. These frequency ranges are independent of the number of Fourier components included in the analysis. For instance, for mode 3 in figure 3.9, NF for the $+2$ harmonic component shows a local minimum around $\Omega = 600$ rad/sec. This "potential $+2$ harmonic resonance" is found for all $n \geq 2$.

4. Modes 7 and 8 at roughly $f = \pm 3216$ Hz behave fundamentally different from the other elastic modes (modes 3 through 6). No n-independent frequencies with low NF are observed.
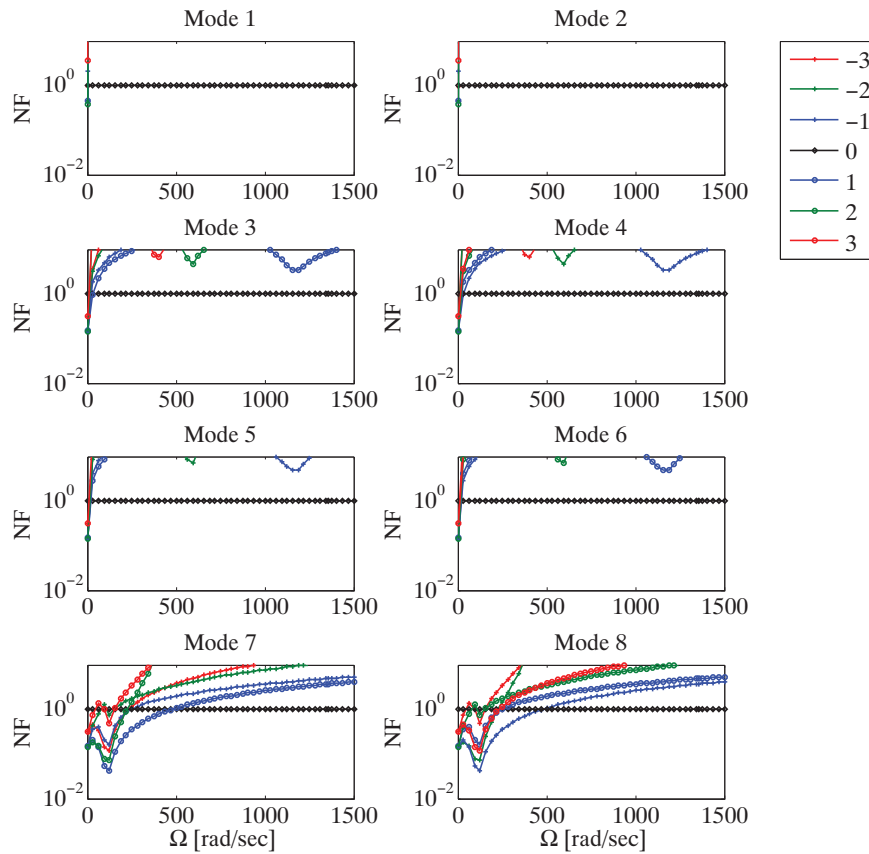
Figure 3.9: Normalization factors, $n = 3$

5. For modes 7 and 8, frequency intervals exist in which NF for one or more harmonic components of the mode shape are smaller than 1. In these frequency intervals, which depend on the number of Fourier components included but are generally located in $\Omega \in [0,600]$ rad/sec, the content of the time-varying part of the mode in the overall mode shape is larger than the fundamental component. These modes are strongly dependent on the relative angular movement between the two gears, and are strongly affected by the time-varying tooth stiffness.
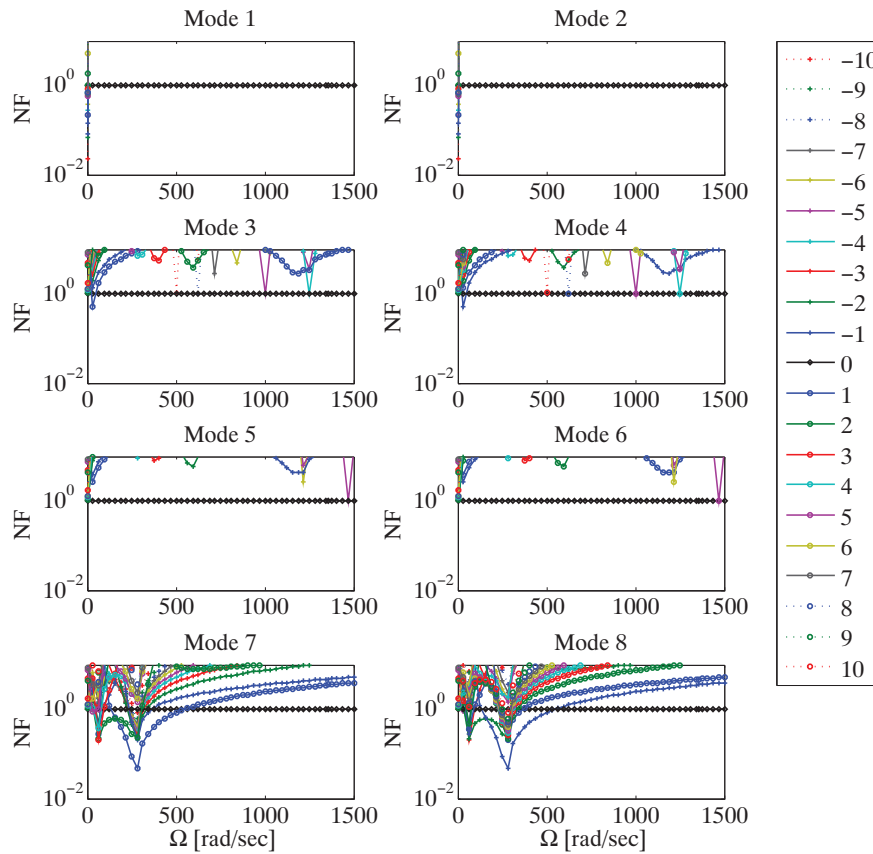
Figure 3.10: Normalization factors, $n = 10$

3.4 Conclusions

The theory of modal analysis of time-varying systems has been applied to a simple spur gear pair with a periodically time-varying gear mesh stiffness. It has been made clear that a large number of terms in the Fourier expansion of the system matrices is necessary in order to yield results of sufficient accuracy. This is a direct result of the jumps in the gear mesh stiffness function. In the cases of flexible rotors with non-symmetrical cross section, flexible rotating discs, and flexible rotating blades, a very reduced number of Fourier

components is needed, normally $n = 2$, as the time-varying coefficients are normally sine and cosine functions.

It has been shown that there exist regions, in which the higher-order parametric contributions to the overall mode shapes will be significant. For the case studied here, these effects were mainly observed at low gear mesh frequencies.

The elastic mode with the highest frequency behaved differently from the other elastic modes. While the two lower modes showed parametric resonance frequencies that were largely independent of the number of Fourier components included in the analysis n, the parametric resonance areas of the high frequency mode strongly depended on n. Overall, the vibrations related to the higher frequency mode seemed to be more sensitive to the time-varying nature of the gear mesh stiffness.

The system studied in this work consisted of a single gear stage. A typical modern wind turbine gearbox consists of one or two planetary stages followed by one or two parallel gear stages, with a total of 8 to 15 gear meshes. When applying the theory of modal analysis of time-varying systems to such a complex system, great care must be taken when interpreting the results. The larger the number of Fourier components needed to expand the periodic time-varying coefficients, the larger the hyper-eigenvalue problem becomes. It means also that it becomes more complicated and complex to physically interpret the basic and parametric mode shapes. Nevertheless, by exploring the definition of NF, the importance of the time-varying part of the mode shapes (parametric modes) can be investigated and quantified as a function of the gear mesh frequency. Compared to time-step integration schemes, the main advantage of the time-varying modal analysis is that it offers an analytical solution to the vibration problem. Therefore a modal truncation is possible, which removes the need for the very short time step used for a numerical integration of a system with high eigenfrequencies. Also the method allows to expand the analysis to the concepts of observability and controllability [69], which offer a quantification of the parametric vibrations.

The focus of this chapter has been to connect an advanced gear mesh stiffness model with a very simple multibody model. In the remaining chapters of this report, a different modeling approach is used. More emphasis will be put on the multibody model and less on the gear mesh stiffness.

Chapter 4

Torsional Multibody Model

This section shows how a torsional model of the 2.3 MW wind turbine gearbox is set up. The method for calculating the gear mesh stiffness described in chapter 2 is used. Tooth modifications have been considered using the exponents $n = 2$ and $m = 2$ in equations (2.35) and (2.36). However only the mean value of the stiffness is used. Compared to the time-varying modal analysis of chapter 3, which deals with only a small part of the wind turbine gearbox, the goal of the model presented in the current chapter is to capture a substantial part of the overall dynamic behavior of the gearbox.

The first step is to establish the equations of motion in order to find the mass matrix $\mathbf{M}$ and stiffness matrix $\mathbf{K}$ to set up the unconstrained, undamped equations of motion for the system.

4.1 Equations of Motion - Shaft

Several textbooks [77, 59] state the mass and stiffness matrix of shaft elements as shown in figure 4.1. The matrices for undamped, free-free torsional
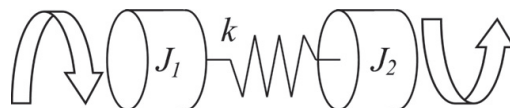

Figure 4.1: Torsional model of a beam

vibrations are

$$\mathbf{M} = \begin{bmatrix} J_1 & 0 \\ 0 & J_2 \end{bmatrix} \text{ and } \mathbf{K} = \begin{bmatrix} k & -k \\ -k & k \end{bmatrix} \tag{4.1}$$

4.2 Equations of Motion - Pair of Gears

The mass and stiffness matrices for a gear pair are easily derived using Newton's equations and Hooke's law. A gear pair is shown in figure 4.2. The
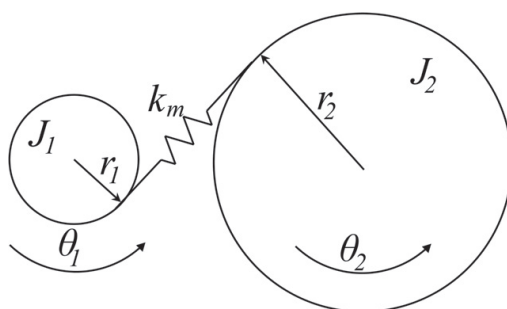

Figure 4.2: Torsional model of a gear pair

force in the gear mesh is called F, which makes the equilibrium equations take the following form:

$$
\begin{aligned}
J_1 \ddot{\theta}_1 &= -Fr_1 \\
J_2 \ddot{\theta}_2 &= -Fr_2
\end{aligned}
\tag{4.2}
$$

In an undamped system, the force F is a function of the elastic deformation of the gears alone. The spring stiffness k_m of the gear mesh is here a linear stiffness (as opposed to a torsional stiffness).

$$F = k_m \left(r_1 \theta_1 + r_2 \theta_2 \right) \tag{4.3}$$

Inserting equation (4.3) into equations (4.2) and rewriting to vector form directly gives the mass and stiffness matrices:

$$J_1\ddot{\theta}_1 + k_m r_1^2 \theta_1 + k_m r_1 r_2 \theta_2 = 0 \tag{4.4}$$

$$J_2\ddot{\theta}_2 + k_m r_1 r_2 \theta_1 + k_m r_2^2 \theta_2 = 0 \tag{4.5}$$

$\Updownarrow$

$$\begin{bmatrix} J_1 & 0 \\ 0 & J_2 \end{bmatrix} \begin{bmatrix} \ddot{\theta}_1 \\ \ddot{\theta}_2 \end{bmatrix} + \begin{bmatrix} k_m r_1^2 & k_m r_1 r_2 \\ k_m r_1 r_2 & k_m r_2^2 \end{bmatrix} \begin{bmatrix} \theta_1 \\ \theta_2 \end{bmatrix} = \begin{bmatrix} 0 \\ 0 \end{bmatrix} \tag{4.6}$$

The close resemblance between equation (4.6) and the matrices of equation (4.1) should be noted. If the gear mesh spring k_m, which is located a distance r_1 from the center of gear 1, is regarded as a torsional spring with the stiffness $k = k_m r_1^2$, and the gear ratio $i = r_2/r_1$ is introduced, the stiffness matrix of equation (4.6) can be written as

$$\mathbf{K} = \begin{bmatrix} k & ik \\ ik & i^2 k \end{bmatrix} \tag{4.7}$$

It is clear, that the gear mesh can be seen as a special beam element that changes the direction of rotation (the off-diagonal components of $\mathbf{K}$ are positive), and multiplies the amplitude of the vibrations by a factor of i, when going from gear 2 to gear 1.

4.3 Equations of Motion - Planetary Stage

The equations of motion for the torsional vibration of a planetary stage as shown in figure 4.3 can be found using the Lagrange function $L = T - U$, where T is the total kinetic energy in the system, and U is the potential energy [59]. The DOFs, which are the rotations of the inertias, are called θ_c, θ_r, θ_{p1}, θ_{p2}, θ_{p3}, and θ_s for the planetary carrier, the ring gear, the three planets, and the sun gear, respectively. In the following equations, for clarity only one planet is considered. The other planets are treated in the same way. The total kinetic energy T of the planetary stage with one planet can be written as

$$T = \frac{1}{2}J_c\dot{\theta}_c^{\,2} + \frac{1}{2}J_r\dot{\theta}_r^{\,2} + \frac{1}{2}J_p\dot{\theta}_p^{\,2} + \frac{1}{2}J_s\dot{\theta}_s^{\,2} \tag{4.8}$$

Because of the connection between the rotation of the planet carrier, and the translation of the planet, the mass of the planet must be included in J_c. This
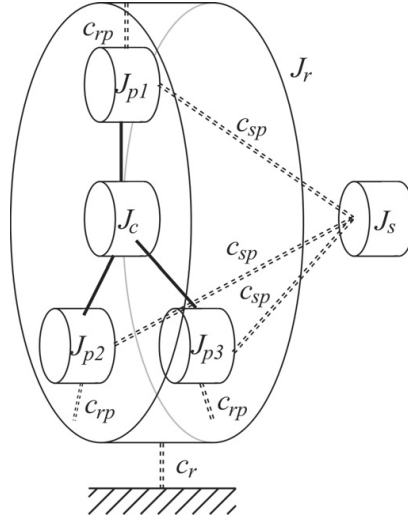
Figure 4.3: Torsional multibody model of a planetary stage. For clarity, the torsional springs are shown as dotted lines

means that $J_c = J_{c,0} + r_c^2 m_p$ for the one-planet system, and $J_c = J_{c,0} + n r_c^2 m_p$ for the n-planet system. $J_{c,0}$ is the inertia of the planet carrier only, m_p is the mass of the planet, and r_c is the distance between the planet and carrier centers.

The total potential energy U is the elastic energy stored in the springs. For a single spring, U can be calculated from the contraction of the spring x using the formula $U = \int cx \, dx = \frac{1}{2} cx^2$, when the spring stiffness c is treated as a constant. For a ring-planet gear mesh, the potential energy is

$$U_{rp} = \frac{1}{2} c_{rp} \Big(r_{bp} \theta_p - r_{br} \theta_r + r_c \cos(\alpha) \theta_c \Big)^2 \tag{4.9}$$

In equation (4.9) r_b denotes the base radius for the gear, α the pressure angle, and r_c the distance from the carrier center to the center of the planets. For a sun-planet gear mesh, the corresponding equation is

$$U_{sp} = \frac{1}{2} c_{sp} \Big(- r_{bs} \theta_s + r_{bp} \theta_p + r_c \cos(\alpha) \theta_c \Big)^2 \tag{4.10}$$

Now the Lagrange function L can be calculated (again only considering one planet):

$$L = T - U \tag{4.11}$$

$$= \frac{1}{2}J_c\dot{\theta}_c{}^2 + \frac{1}{2}J_r\dot{\theta}_r{}^2 + \frac{1}{2}J_p\dot{\theta}_p{}^2 + \frac{1}{2}J_s\dot{\theta}_s{}^2$$

$$- \frac{1}{2}c_{rp}\left(r_{bp}\theta_p - r_{br}\theta_r + r_c\cos(\alpha)\theta_c\right)^2$$

$$- \frac{1}{2}c_{sp}\left(-r_{bs}\theta_s + r_{bp}\theta_p + r_c\cos(\alpha)\theta_c\right)^2 \tag{4.12}$$

For free vibrations, the following equation applies to all coordinates θ:

$$\frac{\mathrm{d}}{\mathrm{d}t}\left(\frac{\partial L}{\partial\dot{\theta}}\right) - \frac{\partial L}{\partial\theta} = 0 \tag{4.13}$$

As an example, the necessary derivatives are calculated below for the planetary carrier. For the ring, the planets, and the sun gear, these calculations are found in Appendix A.

$$\frac{\partial L}{\partial\dot{\theta}_c} = J_c\dot{\theta}_c \Rightarrow \frac{\mathrm{d}}{\mathrm{d}t}\left(\frac{\partial L}{\partial\dot{\theta}_c}\right) = J_c\ddot{\theta}_c \tag{4.14}$$

$$\frac{\partial L}{\partial\theta_c} = -c_{rp}r_c\cos(\alpha)\left(r_c\cos(\alpha)\theta_c - r_{br}\theta_r + r_{bp}\theta_p\right)$$

$$-c_{sp}r_c\cos(\alpha)\left(r_c\cos(\alpha)\theta_c + r_{bp}\theta_p - r_{bs}\theta_s\right) \tag{4.15}$$

Rearranging the terms leads to

$$\frac{\mathrm{d}}{\mathrm{d}t}\left(\frac{\partial L}{\partial\dot{\theta}}\right) - \frac{\partial L}{\partial\theta} = 0 \tag{4.16}$$

$$\Updownarrow$$

$$J_c\ddot{\theta}_c$$

$$+\left((c_{rp} + c_{sp})(r_c\cos(\alpha))^2\right)\theta_c$$

$$+\left(-c_{rp}r_{br}r_c\cos(\alpha)\right)\theta_r$$

$$+\left((c_{rp} - c_{sp})(r_{bp}r_c\cos(\alpha))\right)\theta_p$$

$$+\left(-c_{sp}r_{bs}r_c\cos(\alpha)\right)\theta_s = 0 \tag{4.17}$$

Equation (4.17) and the equivalent equations in Appendix A can be written in vector form, once the DOFs are assembled in a vector $\boldsymbol{\theta} = [\theta_c \; \theta_r \; \theta_{p1} \; \theta_{p2} \; \theta_{p3} \; \theta_s]^T$ for a three-planet system:

$$\mathbf{M}\ddot{\boldsymbol{\theta}} + \mathbf{K}\boldsymbol{\theta} = \mathbf{0} \tag{4.18}$$

All components of the matrices $\mathbf{M}$ and $\mathbf{K}$ are included in equations (4.19) and (4.20), respectively. As expected, the mass matrix is a diagonal (lumped) matrix, and the stiffness matrix is symmetric.

The gearbox housing must be expected to greatly influence the overall dynamic behavior of the gearbox. Through the bearings, lateral vibrations of a shaft can excite housing vibrations. However, since the bearings do not transmit torsional vibrations from shaft to housing, the influence of the housing can be neglected in a torsional model.

Mass matrix for the three-planet planetary stage:

$$\mathbf{M} = \begin{bmatrix} J_c & 0 & 0 & 0 & 0 & 0 \\ 0 & J_r & 0 & 0 & 0 & 0 \\ 0 & 0 & J_p & 0 & 0 & 0 \\ 0 & 0 & 0 & J_p & 0 & 0 \\ 0 & 0 & 0 & 0 & J_p & 0 \\ 0 & 0 & 0 & 0 & 0 & J_s \end{bmatrix} \tag{4.19}$$

Stiffness matrix for the three-planet planetary stage:

$$\mathbf{K} = \begin{bmatrix} 3(c_{rp}+c_{sp})(r_c\cos(\alpha))^2 & -3c_{rp}r_{br}r_c\cos(\alpha) & (c_{rp}-c_{sp})(r_{bp}r_c\cos(\alpha)) & (c_{rp}-c_{sp})(r_{bp}r_c\cos(\alpha)) & (c_{rp}-c_{sp})(r_{bp}r_c\cos(\alpha)) & -3c_{sp}r_c\cos(\alpha)r_{bs} \\ -3c_{rp}r_{br}r_c\cos(\alpha) & c_{rp}r_{br}^2 & -c_{rp}r_{br}r_{bp} & -c_{rp}r_{br}r_{bp} & -c_{rp}r_{br}r_{bp} & 0 \\ (c_{rp}-c_{sp})(r_{bp}r_c\cos(\alpha)) & -c_{rp}r_{br}r_{bp} & (c_{rp}+c_{sp})r_{bp}^2 & 0 & 0 & c_{sp}r_{bp}r_{bs} \\ (c_{rp}-c_{sp})(r_{bp}r_c\cos(\alpha)) & -c_{rp}r_{br}r_{bp} & 0 & (c_{rp}+c_{sp})r_{bp}^2 & 0 & c_{sp}r_{bp}r_{bs} \\ (c_{rp}-c_{sp})(r_{bp}r_c\cos(\alpha)) & -c_{rp}r_{br}r_{bp} & 0 & 0 & (c_{rp}+c_{sp})r_{bp}^2 & c_{sp}r_{bp}r_{bs} \\ -3c_{sp}r_c\cos(\alpha)r_{bs} & 0 & c_{sp}r_{bp}r_{bs} & c_{sp}r_{bp}r_{bs} & c_{sp}r_{bp}r_{bs} & 3c_{sp}r_{bs}^2 \end{bmatrix} \tag{4.20}$$

4.4　Test Rig Modeling

The beam, the gear pair, and the planetary stage are the essential building blocks to build a torsional multibody model of the two gearboxes mounted back-to-back in the test rig. A schematic overview drawing of the system is given in figure 4.4. A total of 33 DOFs were used to model the test rig. In
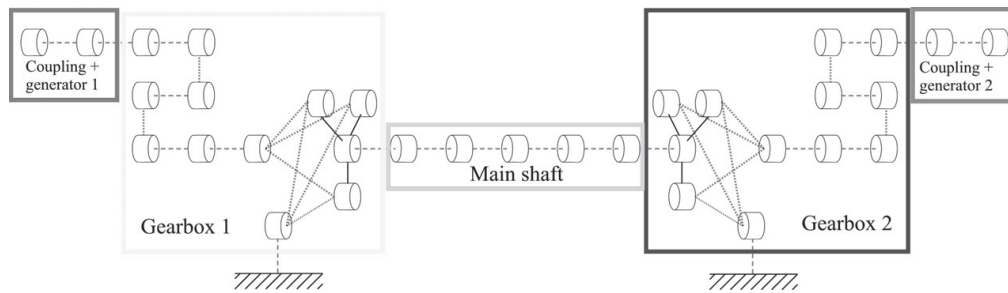

Figure 4.4: Torsional multibody model overview. The solid black lines represent rigid links, while the dashed red lines are flexible torsional springs. The dotted blue lines represent the flexible gear meshes

the figure, the main parts of the test rig are highlighted. The numbering of the nodes and stiffnesses is shown in figure 4.5. When building the test rig
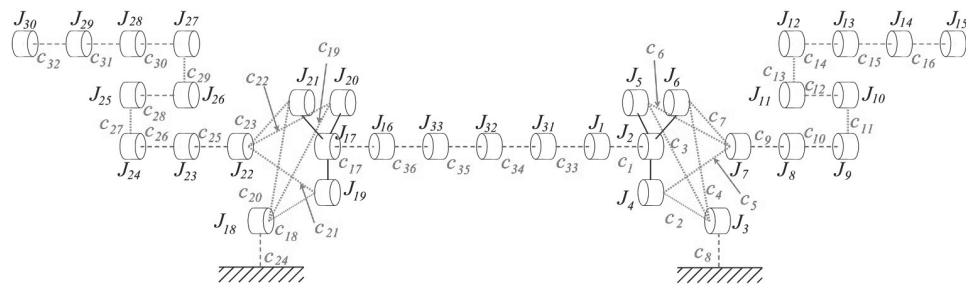

Figure 4.5: Node and stiffness numbering

model, the mass and stiffness matrices $\mathbf{M}$ and $\mathbf{K}$ can be expressed as a sum of the mass and stiffness matrices of each of the elements described above.

For a system containing N elements, this can be expressed as

$$\mathbf{M} = \sum_{i=1}^{N} \mathbf{M}_{\text{sub}}^{i} \quad \text{and} \quad \mathbf{K} = \sum_{i=1}^{N} \mathbf{K}_{\text{sub},i}^{i} \tag{4.21}$$

The sub-matrices of the system are useful when the modal energy distributions are to be calculated, and are necessary for the model updating in section 6.3.

4.5 Conclusions

A torsional model of the test rig has been presented. The model includes two 2.3 MW gearboxes mounted back-to-back, and is expected to correctly simulate the torsional vibrations of the system. The experimental validation of this model is one of the main contributions of this thesis. In the next chapter, the measurements necessary for the model validation are presented.

Chapter 7

Summary and Conclusions

A gear mesh stiffness model, which takes into account the effects of load and grinding corrections as well as the relative gear position along the line of action, has been set up. In the subsequent validation, it was shown that the model is able to reproduce both theoretically and experimentally obtained tooth pair stiffness results found in the literature. A comparison with a commercial software package, KissSoft, again proves the validity of the model, since the gear mesh stiffness functions are nearly identical. The proposed model calculates the effect of load-induced increase of contact ratio. Also this is in good agreement with the KissSoft predictions.

The theory of modal analysis of periodic time-varying systems is well-known, but it has not yet been proven efficient in the field of gear dynamics. An attempt is made here, making this topic one of the major contributions of the work. Using gear data based on the intermediate stage of a 1 MW wind turbine gearbox, the gear mesh stiffness is calculated using the previously validated stiffness model. It is then expanded in a Fourier series and combined with a torsional multibody model with a reduced number of degrees-of-freedom. Under the assumption of constant angular velocity of the gears, the time-varying modal analysis is carried out. It was found that the discontinuities often found in gear mesh stiffness functions significantly increase the necessary number of Fourier components, which in turn increases computation time. However, the method provides possibilities for a modal truncation, and by comparing the stationary and the time-varying parts of the mode shapes, the importance of the parametric modes can be determined.

Using the validated mesh stiffness model, the stiffnesses of all gear meshes in a 2.3 MW wind turbine gearbox are calculated. This includes both external gear meshes and internal meshes as found in the planetary stage of the gearbox. The mean value of the stiffnesses is included in a torsional multibody model of two 2.3 MW gearboxes mounted back-to-back in a test rig. Comparisons with a well-established calculation software (DRESP) is carried out. Some eigenfrequencies show a relatively large difference between the two models, but all such differences can be directly attributed to minor discrepancies in shaft stiffnesses and shaft discretization. Based on this comparison, it is concluded that the proposed model is correctly built, as a large number of the mode shapes and eigenfrequencies from the DRESP model can be recognized.

A measurement campaign has been conducted with the purpose of determining eigenfrequencies for the back-to-back gearbox arrangement. This campaign and the subsequent model validation are further original contributions of this thesis. The eigenfrequencies were found from a series of accelerometer measurements, which included both run-up tests and stationary tests. The measurements also provided a somewhat qualitative description of the associated mode shapes. The test rig arrangement possesses a large number of eigenfrequencies, many of which has a large portion of the total modal energy in the rotational DOF. A load-dependence can be observed in some eigenfrequencies. It is assumed that the elastic strain energy in the corresponding mode shape is stored in components with a load-dependent stiffness, such as bearings, gear meshes, and rubber bushings.

A comparison between simulated and measured eigenfrequencies was carried out. Some torsional eigenfrequencies showed differences of up to 11 per cent. Since this level of correlation was not sufficiently good, an updating technique was employed to adjust the model parameters. As a part of the model updating, weighting functions were used in order to control the change in the parameters. This made it possible for the torsional model to reproduce the measured torsional eigenfrequencies to a degree of accuracy that exceeds the measurement accuracy. A scalar measure of deviation between measured and calculated eigenfrequencies was introduced. The average deviation for the six eigenfrequencies used in the updating procedure drops from 4.7 percent for the purely theoretical model to 0.05 per cent for the updated model.

Bibliography

[1] Walker, H., 1938. "Gear tooth deflection and profile modification". The Engineer, **166** (4319) , pp. 434–436.

[2] Weber, C. and Banaschek, K., 1953. "Formänderung und Profilrücknahme bei gerad- und schrägverzahnten Rädern". Schriftenreihe Antriebstechnik (Heft 11) .

[3] Ziegler, H., 1971. *Verzahnungssteifigkeit und Lastverteilung schrägverzahnter Stirnräder.* PhD thesis, Rheinisch-Westfälische Technische Hochschule Aachen, Germany.

[4] Niemann, G. and Winter, H., 1983 Nachdr. 1989. *Maschinenelemente Band II.* Springer-Verlag, Berlin.

[5] Vijayakar, S., 1991. "A combined surface integral and finite element solution for a three-dimensional contact problem". International Journal for Numerical Methods in Engineering, **31** (3) , pp. 525–545.

[6] Arafa, M. H. and Megahed, M. M., 1999. "Evaluation of spur gear mesh compliance using the finite element method". Proceedings of the Institution of Mechanical Engineers -C- Jnl of Mechanical Engin Science, **213** (6) , pp. 569–580.

[7] International Organization for Standardization, 1996. *ISO 6336, Calculation of load capacity of spur and helical gears, part 1-5.* Genéve, Switzerland.

[8] Deutsches Institut für Normung e. V. *DIN 3990, Tragfähigkeitsberechnung von Stirnrädern, Teil 1-5.* Germany.

[9] Winter, H. and Podlesnik, B., 1983. "Zahnfedersteifigkeit von Stirnradpaaren, Teil 1". Antriebstechnik, **22** (3) , pp. 39–42.

[10] Winter, H. and Podlesnik, B., 1983. "Zahnfedersteifigkeit von Stirnrad-paaren, Teil 2". Antriebstechnik, **22** (5) , pp. 51–58.

[11] Winter, H. and Podlesnik, B., 1983. "Zahnfedersteifigkeit von Stirnrad-paaren, Teil 3". Antriebstechnik, **23** (11) , pp. 43–49.

[12] American Gear Manufacturers Association. *AGMA 2001, Fundamental rating factors and calculation methods for involute spur and helical gear teeth.* USA.

[13] Gregory, R., Harris, S. and Munro, R., 1963. "Torsional motions of pair of spur gears". *Applied Mechanics Convention and Institution of Mechanical Engineers – Proceedings,* **178** , pp. 166–173.

[14] Blankenship, G. W. and Singh, R., 1992. "Comparative study of selected gear mesh interface dynamic models". *Advancing Power Transmission Into the 21st Century and American Society of Mechanical Engineers, Design Engineering Division (Publication) DE,* **43 pt 1** , pp. 137–146.

[15] Velex, P. and Ajmi, M., 2006. "On the modelling of excitations in geared systems by transmission errors". Journal of Sound and Vibration, **290** (3) , pp. 882–909.

[16] Kahraman, A. and Singh, R., 1990. "Non-linear dynamics of a spur gear pair". Journal of Sound and Vibration, **142** (1) , pp. 49–75.

[17] Kahraman, A. and Singh, R., 1991. "Non-linear dynamics of a geared rotor-bearing system with multiple clearances". Journal of Sound and Vibration, **144** (3) , pp. 469–506.

[18] Kahraman, A. and Singh, R., 1991. "Interactions between time-varying mesh stiffness and clearance non-linearities in a geared system". Journal of Sound and Vibration, **146** (1) , pp. 135–156.

[19] Kahraman, A. and Singh, R., 1992. "Dynamics of an oscillator with both clearance and continuous non-linearities". Journal of Sound and Vibration, **153** (1) , pp. 180–185.

[20] Peeken, H., Troeder, C. and Diekhans, G., 1980. "Parametererregte Getriebeschwingungen, Teil 1". VDI-Z, **122** (20) , pp. 869–877.

[21] Peeken, H., Troeder, C. and Diekhans, G., 1980. "Parametererregte Getriebeschwingungen, Teil 2". VDI-Z, **122** (21) , pp. 967–977.

[22] Peeken, H., Troeder, C. and Diekhans, G., 1980. "Parametererregte Getriebeschwingungen, Teil 3". VDI-Z, **122** (22) , pp. 1029–1043.

[23] Peeken, H., Troeder, C. and Diekhans, G., 1980. "Parametererregte Getriebeschwingungen, Teil 4". VDI-Z, **122** (23/24) , pp. 1101–1113.

[24] Velex, P. and Berthe, D., 1989. "Dynamic tooth loads on geared train". *Proceedings of the 1989 International Power Transmission and Gearing Conference: New Technologies for Power Transmissions of the 90's* , pp. 447–454.

[25] Velex, P. and Maatar, M., 1996. "A mathematical model for analyzing the influence of shape deviations and mounting errors on gear dynamic behaviour". Journal of Sound and Vibration, **191** (5) , pp. 629–660.

[26] Ajmi, M. and Velex, P., 2005. "A model for simulating the quasi-static and dynamic behaviour of solid wide-faced spur and helical gears". Mechanism and Machine Theory, **40** (2) , pp. 173–190.

[27] Küçükay, F., 1987. *Dynamik der Zahnradgetriebe.* Springer-Verlag.

[28] Cunliffe, F., Smith, J. D. and Welbourn, D. B., 1974. "Dynamic tooth loads in epicyclic gears.". Journal of Engineering for Industry - Transactions of the ASME, **96** (2) , pp. 578–584.

[29] Seager, D. L., 1975. "Conditions for the neutralization of excitation by the teeth in epicyclic gearing.". J Mech Eng Sci, **17** (5) , pp. 293–298.

[30] Botman, M., 1976. "Epicyclic gear vibrations.". J Eng Ind Trans ASME, **98 Ser B** (3) , pp. 811–815.

[31] Kahraman, A., 1994. "Dynamic analysis of a multi-mesh helical gear train". Journal of Mechanical Design, Transactions Of the ASME, **116** (3) , pp. 706–712.

[32] Kahraman, A., 1994. "Natural modes of planetary gear trains". Journal of Sound and Vibration, **173** (1) , pp. 125–130.

[33] Kahraman, A., 1994. "Load sharing characteristics of planetary transmissions". Mechanism and Machine Theory, **29** (8) , pp. 1151–1165.

[34] Kahraman, A., 1994. "Planetary gear train dynamics". Journal of Mechanical Design, Transactions Of the ASME, **116** (3) , pp. 713–720.

[35] Saada, A. and Velex, P., 1995. "An extended model for the analysis of the dynamic behavior of planetary trains". Transactions of the ASME - R - Journal of Mechanical Design, **117** (2) , pp. 241–246.

[36] Velex, P. and Flamand, L., 1996. "Dynamic response of planetary trains to mesh parametric excitations". Journal of Mechanical Design, Transactions Of the ASME, **118** (1) , pp. 7–14.

[37] Abousleiman, V. and Velex, P., 2006. "A hybrid 3d finite element/lumped parameter model for quasi-static and dynamic analyses of planetary/epicyclic gear sets". Mechanism and Machine Theory, **41** (6) , pp. 725–748.

[38] Abousleiman, V., Velex, P. and Becquerelle, S., 2007. "Modeling of spur and helical gear planetary drives with flexible ring gears and planet carriers". Transactions of the ASME - R - Journal of Mechanical Design, **129** (1) , pp. 95–106.

[39] Parker, R. G., Agashe, V. and Vijayakar, S. M., 2000. "Dynamic response of a planetary gear system using a finite element/contact mechanics model". Transactions of the ASME - R - Journal of Mechanical Design, **122** (3) , pp. 304–310.

[40] Lin, J. and Parker, R., 1999. "Analytical characterization of the unique properties of planetary gear free vibration". Journal of Vibration and Acoustics, Transactions of the ASME, **121** (3) , pp. 316–321.

[41] Lin, J. and Parker, R. G., 1999. "Sensitivity of planetary gear natural frequencies and vibration modes to model parameters". Journal of Sound and Vibration, **228** (1) , pp. 109–128.

[42] LIN, J. and PARKER, R. G., 2002. "Planetary gear parametric instability caused by mesh stiffness variation". Journal of Sound and Vibration, **249** (1) , pp. 129–145.

[43] Parker, R. G. and Lin, J., 2001. Modeling, modal properties, and mesh stiffness variation instabilities of planetary gears. Army Research Lab/-NASA Report ARL-CR-462 or NASA/CR-2001-210939, NASA.

[44] Peeters, J., 2006. *Simulation of dynamic drive train loads in a wind turbine.* PhD thesis, Katholieke Universiteit Leuven, Belgium.

[45] Craig, R. and Bampton, M., 1968. "Coupling of substructures for dynamic analyses". AIAA Journal, **6** (7) , pp. 1313–1319.

[46] Baud, S. and Velex, P., 2002. "Static and dynamic tooth loading in spur and helical geared systems-experiments and model validation". Journal of Mechanical Design, Transactions of the ASME, **124** (2) , pp. 334–346.

[47] Harris, C. and Piersol, A., Eds., 2002. *Harris´ shock and vibration handbook*, 5 ed. McGraw-Hill.

[48] Ewins, D. J., 1984. *Modal testing: Theory and practice.* Research Studies Press Ltd., John Wiley & Sons Inc.

[49] Ognjanović, M. and Ćirić Kostić, S., 2005. "Effects of gear housing modal behaviour at the noise emission". VDI Berichte (1904) , pp. 1767–1772.

[50] Ćirić Kostić, S. and Ognjanović, M., 2003. "Nature and mechanism of modal displacement excitation in gear housing walls". International Conference Power Transmissions '03.

[51] Aoyama, E., Katayama, T., Tange, H., Hirogaki, T., Uenishi, Y., Yamada, T. and Nakata, Y., 2002. "Monitoring of rotational behavior on spiral bevel gear in gear housing using transfer function". *Proceedings of the 2002 International Conference on Noise and Vibration Engineering, ISMA* , pp. 1545–1553.

[52] Chen, Y., 2004. "An investigation of excitation method for torsional testing of a large-scale steam turbine generator". Transactions of the ASME. Journal of Vibration and Acoustics, **126** (1) , pp. 163–167.

[53] Rebbechi, B., Oswald, F. B. and Townsend, D. P., 1991. Dynamic measurements of gear tooth friction and load. Technical Memorandum 103281, Technical Report TR-90-C-023, NASA/AVSCOM.

[54] Oswald, F. B., Townsend, D. P., Rebbechi, B. and Lin, H. H., 1996. "Dynamic forces in spur gears - measurement, prediction, and code validation". *American Society of Mechanical Engineers, Design Engineering Division (Publication) DE,* **88** , pp. 9–15.

[55] Deutsches Institut für Normung e. V. *DIN 3998-1, Benennungen an Zahnrädern und Zahnradpaaren; Allgemeine Begriffe.* Germany.

[56] Deutsches Institut für Normung e. V. *DIN 3999-1, Kurzzeichen für Verzahnungen.* Germany.

[57] Deutsches Institut für Normung e. V. *DIN 3960, Begriffe und Bestimmungsgrößen für Stirnräder (Zylinderräder) und Stirnradpaare (Zylinderradpaare) mit Evolventenverzahnung.* Germany.

[58] Padieth, R., 1978. "Exakte Ermittlung der Zahnform". Antriebtechnik, **17** (10) , pp. 434–436.

[59] Meirovitch, L., 2001. *Fundamentals of Vibrations.* McGraw-Hill.

[60] Schmidt, G., 1973. *Berechnung der Wälzpressung schrägverzahnter Stirnräder unter Berücksichtigung der Lastverteilung.* PhD thesis, Technische Universität München, Germany.

[61] Cornell, R. W., 1981. "Compliance and stress sensitivity of spur gear teeth.". Journal of Mechanical Design, Transactions of the ASME, **103** (2) , pp. 447–459.

[62] Ertz, M., Reister, A. and Nordmann, R., 1995. "Zur Berechnung der Eigenschwingungen von Strukturen mit periodisch zeitvarianten Bewegungsgleichungen". In Schwingungen in rotierenden Maschinen, H. Irretier and R. Nordmann, Eds., vol. III, Springer, Vieweg, pp. 288–296. Braunschweig, Germany.

[63] Xu, J. and Gasch, R., 1995. "Modale Behandlung linearer periodisch zeitvarianter Bewegungsgleichungen". Archive of Applied Mechanics - Ingenieur Archiv, **65** (3) , p. 178.

[64] Boru, F. E. and Irretier, H., 2009. "Numerical and experimental dynamic analysis of a rotor with non-circular shaft mounted in anisotropic bearings". In SIRM 2009 - 8th International conference on vibrations in rotating machines, pp. 1–10. Vienna, Austria.

[65] Irretier, H. and Reuter, F., 1997. "Frequenzgänge rotierender periodisch zeitvarianter Systeme". In Schwingungen in rotierenden Maschinen, H. Irretier and R. Nordmann, Eds., vol. IV, Springer, Vieweg, pp. 113–121. Braunschweig, Germany.

[66] Reuter, F., 1998. "Coupling of elastic and gyroscopic modes of rotating disc structures". In Fifth international conference on rotor dynamics, H. Irretier and R. Nordmann, Eds., pp. 443–455. Darmstadt, Germany.

[67] Santos, I. F. and Saracho, C. M., 2003. "Modal analysis in periodic, time-varying systems with emphasis to the coupling between flexible rotating beams and non-rotating flexible structures". In Proceedings of the Xth International Symposium on Dynamic Problems of Mechanics, pp. 399–404. São Paulo, Brazil.

[68] Christensen, R. and Santos, I., 2005. "Design of active controlled rotor-blade systems based on time-variant modal analysis". Journal of Sound and Vibration, **280** (3-5) , pp. 863–882.

[69] Christensen, R. and Santos, I., 2005. "Modal controllability and observability of bladed disks and their dependency on the angular velocity". Journal of Vibration and Control, **11** (6) , pp. 801–828.

[70] Christensen, R. and Santos, I., 2006. "Active rotor-blade vibration control using shaft-based electromagnetic actuation". Transactions of the ASME. Journal of Engineering for Gas Turbines and Power, **128** (3) , pp. 644–652.

[71] Christensen, R. H. and Santos, I. F., 2006. "Control of rotor-blade coupled vibrations using shaft-based actuation". Shock and Vibration, **13** (4-5) , pp. 255–271.

[72] Irretier, H., 1999. "Mathematical foundations of experimental modal analysis in rotor dynamics". Mechanical Systems and Signal Processing, **13** (2) , pp. 183–191.

[73] Bucher, I. and Ewins, D. J., 2001. "Modal analysis and testing of rotating structures". *Phil. Trans. R. Soc. Lond. A,* **359** , pp. 61–96.

[74] Irretier, H. and Reuter, F., 1991. "Experimentelle Modalanalyse an einer rotierenden Scheibe". In Schwingungen in rotierenden Maschinen,

H. Irretier and R. Nordmann, Eds., vol. I, Springer, Vieweg, pp. 66–77. Braunschweig, Germany.

[75] Bienert, J., 1997. "Anwendung der Strukturmodifikation zur Vorhersage der Kreiselwirkung von symmetrischen und unsymmetrischen Rotoren". In Schwingungen in rotierenden Maschinen, H. Irretier and R. Nordmann, Eds., vol. IV, Springer, Vieweg, pp. 97–104. Braunschweig, Germany.

[76] Santos, I., Saracho, C., Smith, J. and Eiland, J., 2004. "Contribution to experimental validation of linear and non-linear dynamic models for representing rotor-blade parametric coupled vibrations". Journal of Sound and Vibration, **271** (3-5) , pp. 883–904.

[77] Inman, D. J., 1996. *Engineering Vibration*. Prentice Hall.

[78] Sears, F. W., Zemansky, M. W. and Young, H. D., 1987. *University Physics*, 7th ed. Addison-Wesley Publishing Company.

[79] van den Enden, A. W. M. and Verhoeckx, N. A. M., 1989. *Discrete-time signal processing*. Prentice Hall.

[80] Randall, R. B., 1987. *Frequency analysis*, 3rd ed. Brüel & Kjær.

[81] Modak, S. V., Kundra, T. K. and Nakra, B. C., 2002. "Use of an updated finite element model for dynamic design". Mechanical Systems and Signal Processing, **16** (2-3) , pp. 303–322.

[82] Modak, S., Kundra, T. and Nakra, B., 2005. "Studies in dynamic design using updated models". Journal of Sound and Vibration, **281** (3-5) , pp. 943–964.

[83] Modak, S. V., Kundra, T. K. and Nakra, B. C., 2000. "Model updating using constrained optimization". Mechanics Research Communications, **27** (5) , pp. 543–551.

[84] Chen, J. C. and Garba, J. A., 1980. "Analytical model improvement using modal test results.". AIAA Journal, **18** (6) , pp. 684–690.

[85] Collins, J. D., Hart, G. C., Hasselman, T. K. and Kennedy, B., 1974. "Statistical identification of structures.". AIAA J, **12** (2) , pp. 185–190.

[86] Allemang, R. J. and Brown, D. L., 1982. "Correlation coefficient for modal vector analysis.". *Proceedings of the International Modal Analysis Conference & Exhibit* , pp. 110–116.

[87] Mottershead, J. E. and Friswell, M. I., 1993. "Model updating in structural dynamics: A survey". Journal of Sound and Vibration, **167** (2) , pp. 347–375.

Appendix A

Lagrange Derivatives

Partial derivatives of the Lagrange function L to set up the equations of motion for a torsional model of a planetary stage. In the main text, L has been defined for a one-planet system as

$$
\begin{aligned}
L \;=\;& \frac{1}{2}J_c\dot{\theta}_c^{\,2} + \frac{1}{2}J_r\dot{\theta}_r^{\,2} + \frac{1}{2}J_p\dot{\theta}_p^{\,2} + \frac{1}{2}J_s\dot{\theta}_s^{\,2} \\
& -\frac{1}{2}c_{rp}\Big(r_{bp}\theta_p - r_{br}\theta_r + r_c\cos(\alpha)\theta_c\Big)^2 \\
& -\frac{1}{2}c_{sp}\Big(-r_{bs}\theta_s + r_{bp}\theta_p + r_c\cos(\alpha)\theta_c\Big)^2
\end{aligned}
\tag{A.1}
$$

Ring (θ_r):

$$
\frac{\partial L}{\partial \dot{\theta}_r} \;=\; J_r\dot{\theta}_r \Rightarrow \frac{\mathrm{d}}{\mathrm{d}t}\Big(\frac{\partial L}{\partial \dot{\theta}_r}\Big) = J_r\ddot{\theta}_r
\tag{A.2}
$$

$$
\frac{\partial L}{\partial \theta_r} \;=\; c_{rp}r_{br}\Big(r_c\cos(\alpha)\theta_c - r_{br}\theta_r + r_{bp}\theta_p\Big)
\tag{A.3}
$$

Inserting into the equation of motion and rearranging to separate the variables, to prepare for the matrix notation:

$$\frac{\mathrm{d}}{\mathrm{d}t}\left(\frac{\partial L}{\partial \dot{\theta}_r}\right) - \frac{\partial L}{\partial \theta_r} = 0 \tag{A.4}$$

$$\Updownarrow$$

$$
\begin{aligned}
&J_r\ddot{\theta}_r \\
&+\left(-c_{rp}r_{br}r_c\cos(\alpha)\right)\theta_c \\
&+\left(c_{rp}r_{br}^2\right)\theta_r \\
&+\left(-c_{rp}r_{br}r_{bp}\right)\theta_p = 0
\end{aligned} \tag{A.5}
$$

Planet (θ_p):

$$\frac{\partial L}{\partial \dot{\theta}_p} = J_p\dot{\theta}_p \Rightarrow \frac{\mathrm{d}}{\mathrm{d}t}\left(\frac{\partial L}{\partial \dot{\theta}_p}\right) = J_p\ddot{\theta}_p \tag{A.6}$$

$$
\begin{aligned}
\frac{\partial L}{\partial \theta_p} = & -c_{rp}r_{bp}\left(r_c\cos(\alpha)\theta_c - r_{br}\theta_r + r_{bp}\theta_p\right) \\
& +c_{sp}r_{bp}\left(r_c\cos(\alpha)\theta_c - r_{bp}\theta_p - r_{bs}\theta_s\right)
\end{aligned} \tag{A.7}
$$

Inserting into the equation of motion and rearranging to separate the variables, to prepare for the matrix notation:

$$\frac{\mathrm{d}}{\mathrm{d}t}\left(\frac{\partial L}{\partial \dot{\theta}_p}\right) - \frac{\partial L}{\partial \theta_p} = 0 \tag{A.8}$$

$$\Updownarrow$$

$$
\begin{aligned}
&J_p\ddot{\theta}_p \\
&+\left((c_{rp} - c_{sp})r_{bp}r_c\cos(\alpha)\right)\theta_c \\
&+\left(-c_{rp}r_{bp}r_{br}\right)\theta_r \\
&+\left((c_{rp} + c_{sp})r_{bp}^2\right)\theta_p \\
&+\left(c_{sp}r_{bp}r_{bs}\right)\theta_s = 0
\end{aligned} \tag{A.9}
$$

Sun (θ_s):

$$\frac{\partial L}{\partial \dot{\theta}_s} = J_s \dot{\theta}_s \Rightarrow \frac{\mathrm{d}}{\mathrm{d}t}\left(\frac{\partial L}{\partial \dot{\theta}_s}\right) = J_s \ddot{\theta}_s \tag{A.10}$$

$$\frac{\partial L}{\partial \theta_s} = c_{sp} r_{bs} \left(r_c \cos(\alpha)\theta_c - r_{bp}\theta_p - r_b\theta_s \right) \tag{A.11}$$

Inserting into the equation of motion and rearranging to separate the variables, to prepare for the matrix notation:

$$\frac{\mathrm{d}}{\mathrm{d}t}\left(\frac{\partial L}{\partial \dot{\theta}_s}\right) - \frac{\partial L}{\partial \theta_s} = 0 \tag{A.12}$$

$\Updownarrow$

$$J_s \ddot{\theta}_s$$
$$+\left(- c_{sp} r_{bs} r_c \cos(\alpha) \right)\theta_c$$
$$+\left(c_{sp} r_{bs} r_{bp} \right)\theta_p$$
$$+\left(c_{sp} r_{bs}^2 \right)\theta_s = 0 \tag{A.13}$$

Appendix B

Frequency Resolution with Overlap and Averaging

In figure B.1, a signal of length T has been cut up into Z blocks with an overlap of X, with X in the interval [0,1]. It is seen that the length T of the
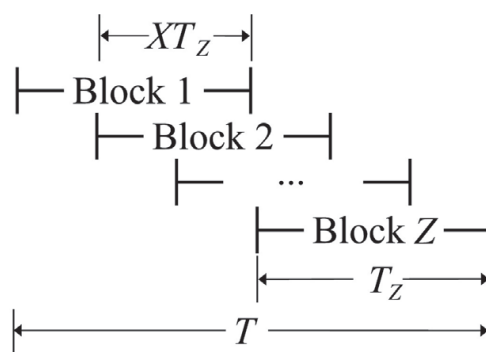

Figure B.1: Signal analysis using overlap and averaging

total signal can be written as the sum of the lengths of the Z blocks minus the $Z-1$ overlap zones. An overlap zone has the length XT_Z. For a signal block of length T_Z, the frequency resolution is

$$\Delta f = \frac{1}{T_Z} \tag{B.1}$$

This will also be the frequency resolution of the full signal, when using overlap and averaging. Now T_Z is found:

$$
\begin{aligned}
T &= ZT_Z - X(Z-1)T_Z & \text{(B.2)} \\
&= T_Z(Z - XZ + X) & \text{(B.3)} \\
&= T_Z(1 - 1 + Z - XZ + X) & \text{(B.4)} \\
&= T_Z(1 + (Z-1)(1-X)) & \text{(B.5)}
\end{aligned}
$$

$$
\Rightarrow T_Z = \frac{T}{1 + (Z-1)(1-X)} \tag{B.6}
$$

Equation (B.6) is inserted in (B.1) which gives

$$
\Delta f = \frac{1 + (Z-1)(1-X)}{T} \tag{B.7}
$$

Appendix C

Torsional-Lateral Vibration Coupling

A non-dimensional torsional-lateral vibration model of a single gear pair is shown in figure C.1(a).
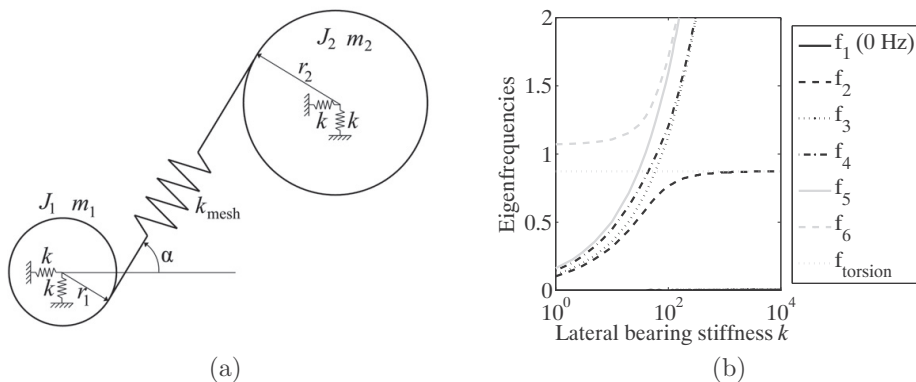

Figure C.1: (a) Example system model, and (b) eigenfrequencies

The mass moments of inertia of the two gears are $J_1 = 1$ and $J_2 = 2$, the masses are $m_1 = 1$ and $m_2 = 2$, the base radii are $r_1 = 1$ and $r_2 = 2$, the pressure angle is $\alpha = 45°$, and the gear mesh stiffness is $k_{\mathrm{mesh}} = 10$. In figure C.1(b) the non-dimensional eigenfrequencies are shown as a function of the lateral bearing stiffnesses k. When the lateral bearing stiffness $k \to \infty$, no motions in the lateral directions are possible, and the model is purely

torsional. With decreasing k, lateral motion is allowed, and the coupling between the lateral and the torsional DOFs becomes important - both the eigenfrequencies and the corresponding mode shapes will be different from the torsional model. For $k \to \infty$, the first non-zero eigenfrequency converges towards the frequency marked f_{torsion} in figure C.1(b).